Radiative-convective models of the atmospheres of Uranus and Neptune: heating sources and seasonal effects

Gwenaël Milcareck, Sandrine Guerlet, Franck Montmessin, Aymeric Spiga, Jeremy Leconte, Ehouarn Millour, Noe Clement, Leigh N Fletcher, Michael T Roman, Emmanuel Lellouch, et al.

A&A, 686, A303 (2024)
https://doi.org/10.1051/0004-6361/202348987

Astronomy & Astrophysics

Radiative-convective models of the atmospheres of Uranus and Neptune: Heating sources and seasonal effects

Gwenaël Milcareck[1,2], Sandrine Guerlet[1,3], Franck Montmessin[2], Aymeric Spiga[1], Jérémy Leconte[4], Ehouarn Millour[1], Noé Clément[4], Leigh N. Fletcher[5], Michael T. Roman[5], Emmanuel Lellouch[3], Raphaël Moreno[3], Thibault Cavalié[4,3], and Óscar Carrión-González[3]

[1] Laboratoire de Météorologie Dynamique/Institut Pierre-Simon Laplace (LMD/IPSL), Sorbonne Université, CNRS, École Polytechnique, Institut Polytechnique de Paris, École Normale Supérieure (ENS), PSL Research University, 4 place Jussieu BC99, 75005 Paris, France
e-mail: gwenael.milcareck@lmd.ipsl.fr
[2] Laboratoire Atmosphères, Milieux, Observations spatiales (LATMOS), IPSL, Observatoire de Versailles St-Quentin-en-Yvelines, Université de Versailles St-Quentin-en-Yvelines, CNRS, 11 boulevard d'Alembert, 78280 Guyancourt, France
[3] Laboratoire d'Etudes Spatiales et d'Instrumentation en Astrophysique (LESIA), Observatoire de Paris, CNRS, Sorbonne Université, Université Paris-Diderot, Meudon, France
[4] Laboratoire d'Astrophysique de Bordeaux, Université de Bordeaux, CNRS, B18N, allée Geoffroy Saint-Hilaire, 33615 Pessac, France
[5] School of Physics & Astronomy, University of Leicester, University Road, Leicester LE1 7RH, UK

Received 17 December 2023 / Accepted 30 March 2024

ABSTRACT

Context. The observations made during the Voyager 2 flyby have shown that the stratosphere of Uranus and that of Neptune are warmer than expected by previous models. In addition, no seasonal variability of the thermal structure has been observed on Uranus since Voyager 2 era and significant subseasonal variations have been revealed on Neptune.
Aims. In this paper, we evaluate different realistic heat sources that can induce sufficient heating to warm the atmosphere of these planets and we estimate the seasonal effects on the thermal structure.
Methods. The seasonal radiative-convective model developed by the Laboratoire de Météorologie Dynamique was used to reproduce the thermal structure of these planets. Three hypotheses for the heating sources were explored separately: aerosol layers, a higher methane mole fraction, and thermospheric conduction.
Results. Our modelling indicates that aerosols with plausible scattering properties can produce the requisite heating for Uranus, but not for Neptune. Alternatively, greater stratospheric methane abundances can provide the missing heating on both planets, but the large values needed are inconsistent with current observational constraints. In contrast, adding thermospheric conduction cannot warm the stratosphere of both planets alone. The combination of these heat sources is also investigated. In the upper troposphere of both planets, the meridional thermal structures produced by our model are found inconsistent with those retrieved from Voyager 2/IRIS data. Furthermore, our models predict seasonal variations should exist within the stratospheres of both planets while observations showed that Uranus seems to be invariant to meridional contrasts and only subseasonal temperature trends are visible on Neptune. However, a warm south pole is seen in our simulations of Neptune as observed since 2003.

Key words. radiative transfer – planets and satellites: atmospheres – planets and satellites: gaseous planets

1. Introduction

Located at 19 and 30 AU respectively from the Sun, Uranus and Neptune are known as cold worlds. The irradiance received at the top of their atmospheres is indeed particularly low: it is 3.69 W m^{-2} for Uranus and 1.51 W m^{-2} for Neptune (on Earth, it is 1361 W m^{-2}). With an albedo of 0.30 and 0.29 for Uranus (Pearl et al. 1990) and Neptune (Pearl & Conrath 1991), respectively, the energy balance implies an absorbed energy flux of 0.64 W m^{-2} for Uranus and 0.27 W m^{-2} for Neptune. These planets differ in their internal energy flux: it is 0.042 ± 0.047 W m^{-2} at most for Uranus (Pearl et al. 1990) while it is estimated at 0.43 ± 0.09 W m^{-2} on Neptune (Pearl & Conrath 1991). Thus, the internal energy flux is greater than the absorbed solar energy in the case of Neptune. With an obliquity of 28.32°, seasonal variations are expected on Neptune. In the case of Uranus, its obliquity of 97.77° means that its rotation axis is almost on its orbital plane and thus, on an annual average, Uranus receives a greater solar flux at the poles than at the equator, unlike the other planets of the Solar System. In summary, these two planets are characterised by low sunlight and long orbital periods (~84 terrestrial years for Uranus and ~165 yr for Neptune), by very marked seasonal variations in irradiance (especially for Uranus), and, in the case of Neptune, strong competition between internal energy flux and absorbed solar flux. These differences impact the energy balance of these planets and therefore their atmospheric temperatures.

Temperature measurements are notably difficult due to the distance and the low infrared radiation emitted by these planets. The most precise measurements of the upper tropospheric temperature structure come from the Voyager 2 flyby. The radio-occultation experiment provided 1D profiles on Uranus

at latitude 2–6° S during northern winter solstice at ~271° in solar longitude (Ls; Lindal et al. 1987) and at latitude 59–62° N during northern autumn (Ls ≃ 235°) on Neptune (Lindal 1992) (see Fig. 1). At 1000 hPa, the temperatures reach ~76 K on Uranus and ~71 K on Neptune. Temperature profiles derived from disk-averaged spectra from the *Spitzer* Infrared Spectrometer for Uranus (Orton et al. 2014), the Infrared Space Observatory for Neptune (Burgdorf et al. 2003), and AKARI (Fletcher et al. 2010b) confirm the temperature observed in the troposphere by Voyager 2 (Fig. 1).

Near 100 hPa, a particularly cold tropopause has been observed by Voyager 2. From radio-occultations, the minimum is 53 K on Uranus and 52 K for Neptune. These temperatures are cold enough for methane to condense. IRIS (Infrared Interferometer Spectrometer and Radiometer) observations from Voyager 2 reveal a complex meridional thermal structure near the tropopause for Uranus (Flasar et al. 1987; Conrath et al. 1998; Orton et al. 2015) and Neptune (Conrath et al. 1989, 1991, 1998; Fletcher et al. 2014). On zonal-mean temperatures maps, an equatorial maximum and a local minimum at mid-latitudes in each hemisphere are observed for both planets.

The stratosphere of both planets has been observed by Voyager 2, space-based and ground-based observatories. Radio occultations from Voyager 2 indicate a temperature of the order of ~80 K at 1 hPa on Uranus and ~125 K at the same level on Neptune. The Voyager 2 PhotoPolarimeter Subsystem (PPS) experiment provided information on temperatures in the uranian lower-stratosphere near 1 hPa at 68.9°N (Lane et al. 1986; West et al. 1987) through a UV stellar occultation. Assuming an aerosol-free atmosphere, the PPS temperature retrieval showed a lower stratosphere warmer by 10 K at ~3 hPa than temperature measurements from radio occultation. Greathouse et al. (2011) and Fletcher et al. (2014) explored meridional temperature variations in Neptune's stratosphere with thermal-infrared images from Keck/Long Wavelength Spectrometer (Keck/LWS) in 2003, Gemini-N/MICHELLE in 2005, VLT Imager and Spectrometer for mid-Infrared (VLT/VISIR) in 2006, Gemini-S/Thermal-Region Camera Spectrograph (Gemini-S/TReCS), and Gemini-N/Texas Echelon Cross Echelle Spectrograph (Gemini-N/TEXES) in 2007. Assuming a spatially constant methane abundance, the stratospheric temperature seems to have been latitudinally isothermal since the Voyager 2 flyby. However, Roman et al. (2022) showed important spatial and temporal variations in the meridional temperature. On Uranus, Roman et al. (2020) suggest that the meridional temperature gradient displays a similar structure to that seen at the tropopause. In the upper stratosphere, UltraViolet Spectrometer (UVS) measurements from Voyager 2 and ground-based stellar occultations showed that this region is particularly hot (on average 150 K at 1 Pa for both planets). However, observations from Voyager 2 and from Earth are inconsistent for both planets. Temperatures measured from Earth are lower than those from Voyager 2 and vary very strongly vertically. Temperature differences can reach 100 K at 1 Pa (Saunders et al. 2023).

To interpret the observed temperature profiles, several radiative-convective equilibrium models have been built and used. The simulated stratospheric temperatures are, by far, too cold compared to the observed ones. The temperature mismatch can reach 30 K in the lower-stratosphere for both planets (Wallace 1983; Appleby 1986; Friedson & Ingersoll 1987; Marley & McKay 1999; Greathouse et al. 2011; Li et al. 2018). This 'energy crisis' (Friedson & Ingersoll 1987) is also present in the thermosphere where there are several hundred Kelvin differences between observations and models (Melin et al. 2019). Many hypotheses have been explored to explain this difference in the stratosphere and thermosphere. Appleby (1986) concluded that the presence of a 'continuum absorber' in the stratosphere – which may be aerosols – could significantly contribute to the energy balance on Uranus but not entirely on Neptune. However, Marley & McKay (1999) showed that adding stratospheric hazes based on the assumption of spherical Mie scattering particles did not warm this region appreciably on Uranus. On Neptune, the same conclusion was established (Moses et al. 1995). Alternatively, a heat flux from an unknown source in the thermosphere (Stevens et al. 1993) that conducts heat to lower levels is not sufficient to warm the stratosphere of Uranus (Marley & McKay 1999) and Neptune (Wang 1993). On Uranus, by adding a small abundance of methane in the lower thermosphere, Marley & McKay (1999) managed to reconcile the observed and modelled temperatures, as in this scenario the stratosphere is warmed by the methane that radiates downwards (Marley & McKay 1999). However, this scenario implies elevated methane abundance values at homopause levels that are inconsistent with Voyager 2 and ground-based observations.

Previous radiative-convective models predicted that Uranus' stratospheric temperatures should undergo seasonal variations over the course of its 84-year orbital period (Wallace 1983; Friedson & Ingersoll 1987; Conrath et al. 1990). Nonetheless, no similar trend has been observed since the Voyager 2 flyby (Roman et al. 2020) except on stellar occultations where an apparent seasonal variation is possible in the high stratosphere (Young et al. 2001; Hammel et al. 2006). On the contrary, the temperature has changed considerably on Neptune since the Voyager 2 era. Significant sub-seasonal variations in the stratosphere have been discovered that could be related to solar activity (Roman et al. 2022) or inertia-gravity waves (Hammel et al. 2006; Uckert et al. 2014). At higher pressures, models predict limited seasonal effects on temperatures near the tropopause (Wallace 1984), and the thermal structure seems to have remained invariant since the Voyager 2 flyby (Orton et al. 2015; Roman et al. 2020), except at the poles (Fletcher et al. 2014).

Understanding the origin of the energy crisis on the ice giants is one of the current major challenges in planetary science. Current 1D radiative-convective models do not reproduce the observed temperature structure or the seasonal variability without adding one or more heating sources. To reproduce the thermal structure of the atmosphere of Uranus and Neptune and its seasonal variability, a seasonal radiative–convective model designed for ice giants is introduced in Sect. 2 with a description of the different parameters used. The temperature profile obtained with our clear-sky model is described in Sect. 3. Section 4 explores several additional heat sources that can warm the stratosphere of both planets. The simulated meridional temperature structure is discussed and compared with the observations in Sect. 5, along with the expected seasonal variability.

2. Methodology

Here, we describe the 1D seasonal radiative–convective equilibrium model tailored for ice giants developed at Laboratoire de Météorologie Dynamique, which aims at understanding the radiative heat sources, the seasonal variability and the thermal structure of Uranus' and Neptune's atmospheres. This model was previously used to simulate the radiative forcing on exoplanets (Wordsworth et al. 2010; Turbet et al. 2016) and, more recently, on Jupiter and Saturn (Guerlet et al. 2014, 2020).

Radiative transfer equations are solved in a column of atmosphere discretized in layers using the two-stream approximation, including multiple scattering as proposed by Toon et al. (1989) and depending on opacity sources that control the heating and cooling rates. In addition to these opacity sources, a radiative flux at the bottom corresponding to the measured internal heat flux is also added in the case of Neptune (not for Uranus, as it is negligible). As suggested by Zhang (2023a,b), the internal heat flux in ice giants could vary with latitude and even fluctuate over time; however, this effect has never been quantified and we did not explore this possibility in our study. To emulate convective mixing, a convective adjustment scheme relaxes the temperature profile towards the adiabatic lapse rate (Hourdin et al. 1993) if an unstable lapse rate is encountered during a simulation. The tropospheric lapse rate is controlled by the standard gravity and the heat capacity fixed at one value. We choose to fix the heat capacity at the value calculated at 3000 hPa (corresponds to the bottom of our model) by using the temperature observed and the abundance of hydrogen for a given ortho:para ratio, helium and methane at this level. On Uranus, a heat capacity of 8600 $J\,K^{-1}\,kg^{-1}$ is found, consistent with the "intermediate" ortho:para ratio case from Massie & Hunten (1982). On Neptune, the heat capacity is chosen for H_2 at equilibrium and set at 9100 $J\,K^{-1}\,kg^{-1}$.

Orbital and planetary settings are added to take seasonal effects on temperature into account. The most important parameter is the obliquity, which is set to 97.77° for Uranus and 28.32° for Neptune. Because Uranus and Neptune have radiative time constants ranging from years to decades (Conrath et al. 1990, 1998; Li et al. 2018), a daily averaged solar flux is considered and calculations of the radiative heating and cooling rates are performed typically once every 25 planetary days.

All seasonal radiative-convective simulations presented in this paper employ a pressure grid consisting of 48 levels between 3000 hPa and 5 Pa which covers the upper troposphere and the lower stratosphere. The radiative spin-up is ensured by running 30 Uranian years and 16 Neptunian years. Regarding the radiative forcings, all opacity contributions are separated into two parts: a thermal infrared one (10–3200 cm^{-1}) which controls the cooling rate and a visible one (2020–33 300 cm^{-1}) which controls the heating rate. Like gas giant planets, radiative cooling results from collision-induced absorption (mainly H_2–H_2 and H_2–He) in the thermal infrared in the lower atmosphere along with thermal emission by the main hydrocarbons (CH_4, C_2H_2, C_2H_6) in the stratosphere. Radiative heating results from the absorption of visible and near-infrared solar photons by methane and collision-induced absorption in the lower atmosphere (Conrath et al. 1990, 1998; Li et al. 2018). The effect of clouds and hazes are considered later in Sect. 4.1.

Thermal emission and visible/near-infrared absorption by hydrocarbons are key to the radiative cooling and heating in ice giant atmospheres. As line-by-line calculations are too time-consuming for model applications, correlated-k coefficients for different spectral bands and temperature–pressure values are pre-calculated offline (Goody et al. 1989; Wordsworth et al. 2010). The k-distribution model was obtained as described by Guerlet et al. (2014) for Saturn with the same compounds. Briefly, we start by computing the high-resolution spectra of the absorption coefficients $k(\nu)$ of hydrocarbons (CH_4, C_2H_2, C_2H_6) line-by-line from the spectroscopic data of HITRAN 2016 and Rey et al. (2018) according to their vertical distribution (Fig. 2) and their methane isotope content (CH_3D, ^{13}C) on a rough temperature-pressure grid (9 values between 40 and 190 K and 12 layers between 10^6 and 0.1 Pa). Then, the spectra are discretized

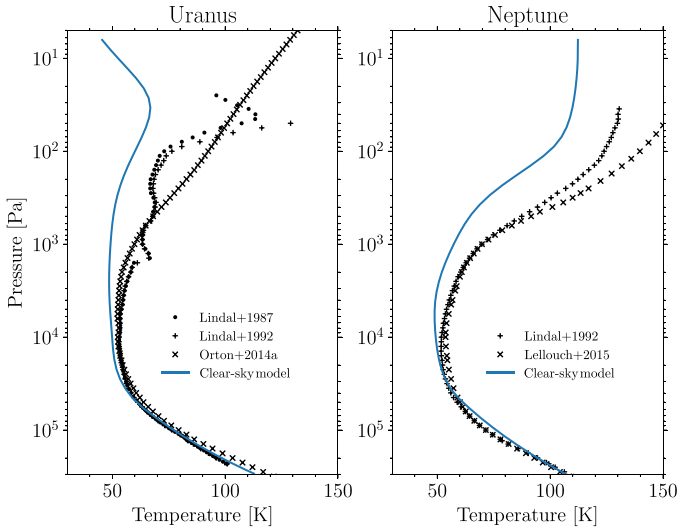

Fig. 1. Temperature simulated by the clear-sky model in blue on Uranus (left) and Neptune (right) at the same latitude and solar longitude as the observations (see text). Observed temperature profiles are from Lindal et al. (1987) (black dots), Lindal (1992) (black plus), Orton et al. (2014) (black cross) for Uranus and Lellouch et al. (2015) (black cross) for Neptune.

into several spectral bands (20 bands for the thermal part and 26 bands in the visible part) between 0.3 and 1000 µm which results from a good compromise between bandwidth and number of bands in order to maintain good precision and a fairly short reading time. For each spectral band and T-p value, high-resolution absorption coefficients $k(\nu)$ are sorted by strength, then converted into a cumulative probability function $g(k)$ (with g varying from 0 to 1), and finally this function is inverted to obtain $k(g)$. This is now a smooth function that replaces $k(\nu)$ and can be integrated over typically 16 Gauss points (8 sampled between 0 and 0.95, plus 8 sampled between 0.95 and 1). Like Guerlet et al. (2014), H_2-broadened coefficients are used instead of air-broadened coefficients for methane and ethane (Halsey et al. 1988; Margolis 1993). During a GCM run, these tabulated coefficients are interpolated at the temperature computed by the model at a given time step, at each pressure level. Non-local thermodynamic equilibrium effects from CH_4 on the temperature are not taken into account because it starts to be significant at pressures lower than 3 Pa for Uranus and 0.5 Pa for Neptune (Appleby 1990), which is above the top boundary of our model. We note that all opacity sources (not only the hydrocarbon ones) are calculated on the spectral bands used by the k-distribution model.

We consider collision-induced absorption (CIA) from H_2–H_2 (Borysow 1991; Zheng & Borysow 1995; Borysow et al. 2000; Fletcher et al. 2018), H_2–He (Borysow et al. 1989; Borysow & Frommhold 1989), H_2–CH_4 (Borysow & Frommhold 1986), He–CH_4 (Taylor et al. 1988) and CH_4–CH_4 (Borysow & Frommhold 1987) according to the vertical distribution of each species (Fig. 2). For H_2–H_2, H_2–He and H_2–CH_4 data, the hydrogen ortho–para ratio is set to the equilibrium as observed (on average) on both planets.

Rayleigh scattering following the method described in Hansen & Travis (1974) from the three main gases (H_2, He, CH_4) is included. Raman scattering by molecular hydrogen is neglected because its optical depth is lower that of Rayleigh scattering (Sromovsky 2005) and the heating and cooling rate of Rayleigh scattering is already much lower than hydrocarbons

or CIA contributions (100–1000 times lower). CIA and Rayleigh scattering are interpolated on the same grid of the *k*-distribution model (pressure, temperature and wavelength).

The abundance of methane on Uranus and Neptune is known to vary with latitude and altitude. Indeed, in the troposphere of Neptune, the molar fraction of methane at the equator reaches 6 to 8% while at the poles, it decreases to 2 to 4% (Karkoschka & Tomasko 2011; Irwin et al. 2019). On Uranus, the gradient is less marked with a methane mole fraction reaching 3 to 4% at the equator and ∼1% at the poles (Karkoschka & Tomasko 2009; Sromovsky et al. 2019). This latitudinal variation is accompanied by a vertical variation linked to the condensation of methane near 1000 hPa and to the photochemistry, eddy and molecular diffusion in the middle and upper atmosphere. On Uranus, due to a more stratified atmosphere, the methane homopause exists at higher pressures (between 10 and 1 Pa) than on Neptune (between 10^{-2} and 10^{-3} Pa; Moses et al. 2018). These variations have the consequence of strongly playing on the competition between the different sources of opacity according to latitude and altitude. The detailed examination of methane's vertical profile can be found in Sect. 4.2. In the case of the model used here, only variations in altitude are taken into account and the methane is assumed to be horizontally uniform and constant over time. For Uranus, the methane mole fraction profile below the 100 Pa level (3.2%) from Lellouch et al. (2015) is combined with the annual average profile from the photochemical model of Moses et al. (2018) above the 100 Pa level (Fig. 2). On Neptune, the methane deep tropospheric value is set to 4% based on latitudinally averaged retrieved values by Irwin et al. (2019); near the condensation level, the profile from Lellouch et al. (2015) is used and above this level, the annual average profile from Moses et al. (2018) is chosen. We take this variation on the abundance of H_2 and He into account, and the molar fraction of He/H_2 is fixed at 0.15/0.85 for both planets (Conrath et al. 1987; Burgdorf et al. 2003). Concerning the vertical distribution of hydrocarbons (C_2H_2, C_2H_6, CH_3D, ^{13}C), they are set to an annual-averaged profile derived from the photochemical model of Moses et al. (2018). Variations in chemical distributions are predicted by photochemical models which alter the heating and cooling rates but the effect is expected to be secondary to direct variation in seasonal insolation at the pressures considered.

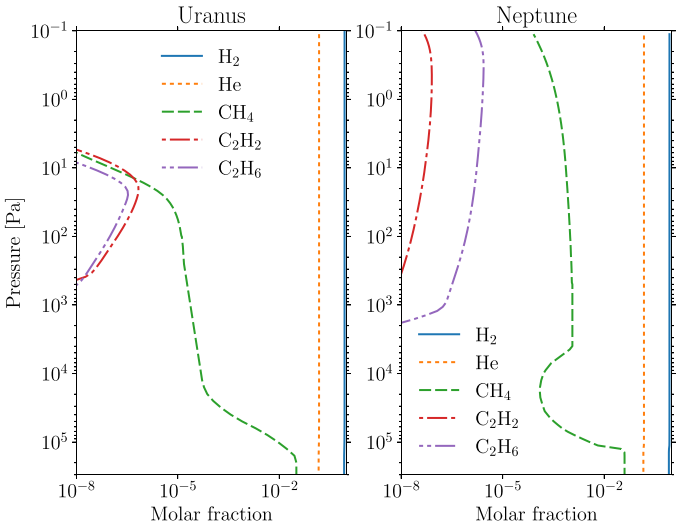

Fig. 2. Vertical molar fraction of the gases on Uranus (left) and Neptune (right) used by the model. Collision-induced absorptions and emissions of H2 and He contribute to radiative heating and cooling throughout the entire atmospheric column, as absorption and emission by methane (except on Uranus, where its abundance becomes insignificant at pressures below ∼10 Pa). The other hydrocarbons are active only in the stratosphere for pressures between ∼1 hPa and ∼7 Pa on Uranus and below than ∼10 hPa on Neptune.

3. Vertical thermal structure: Clear-sky models

Using our 1D radiative–convective model with the parameters described above, we simulated temperature profiles for both planets at the latitudes and solar longitudes corresponding to Voyager 2 radio-occultation profiles. The temperature profiles that derived from Voyager 2 were obtained at 2–6°S and Ls ≃ 271° for Uranus (Lindal et al. 1987; Lindal 1992) and at 59–62°N and Ls ≃ 235° for Neptune (Lindal 1992). We caution that the Lindal (1992) Voyager 2 temperature profile of Neptune was derived assuming a He/H2 ratio of 0.19/0.81 that is higher than the more recently derived 0.15/0.85 ratio (Burgdorf et al. 2003). Using a lower He/H2 ratio in the radio-occultation data analysis would lead to a temperature profile colder by only a few Kelvins, and would not change our conclusions. To complete data in the stratosphere for comparison purposes, the globally averaged temperatures retrieved by Orton et al. (2014) at Ls ≃ 0° for Uranus and Lellouch et al. (2015) at Ls ≃ 279° for Neptune are taking into account. The simulated temperature profiles obtained here are shown in Fig. 1.

The predicted tropospheric temperatures for both planets are similar as expected. This similarity is due to the lack of internal heat flux on Uranus and to the excess in the case of Neptune. Sensitivity tests were performed by parameterising the internal energy flux at the upper and lower limits estimated by Pearl et al. (1990); Pearl & Conrath (1991). On Uranus, the tropospheric temperature obtained at 3000 hPa is warmer by 2 K and on Neptune, it is 5 K warmer (resp. colder) using the high (resp. lower) limit of 0.53 W m^{-2} (resp. 0.38 W m^{-2}). The tropospheric temperatures on Neptune are thus sensitive to the internal heat flux. Concerning their stratosphere, as in previous studies, an important gap called 'energy crisis' exists between the temperature retrieved by the observations and the simulated ones. The difference begins at the top of the troposphere on Uranus (∼500 hPa) and at the tropopause on Neptune (∼100 hPa). The temperature mismatch reaches ∼70 K on Uranus at 10 Pa and ∼25 K on Neptune at 100 Pa. Our model predicts also that Neptune's stratosphere is warmer than Uranus' despite its larger distance to the Sun. For instance, at 1 hPa, our model predicts that Neptune is 35 K warmer than Uranus. This can be explained by a significantly higher abundance of methane in Neptune's stratosphere (1.3×10^{-5} on Uranus and 1×10^{-4} on Neptune at 1 hPa), implying a larger heating rate. This is consistent with the results of Li et al. (2018) who computed the different contributions of the gaseous opacity sources to the heating and cooling rates: at pressures lower than 50 hPa, methane is the dominant heating source. Regarding the cooling rates, on Uranus, they are dominated by the CIA opacities throughout the atmosphere while on Neptune, CIA opacities control the cooling rates at pressures higher than 1–2 hPa and hydrocarbons are the dominant contributors at lower pressures. We note that like in our simulations, Li et al. (2018) (who did not take haze opacities into account) reported a heating deficit in both planets' stratospheres.

To further evaluate our results, we computed the Bond albedo, based on simulations performed at all latitudes. Pearl et al. (1990) and Pearl & Conrath (1991) inferred a Bond albedo of 0.30 ± 0.05 and 0.29 ± 0.05 based on Voyager 2 observations for Uranus and Neptune, respectively. Our values of 0.27 and

0.25 are in rough agreement with the ones derived from observations. We note however that the reanalysis of full-disk reflectivity data from Voyager 2 flyby hints at a Bond albedo that may be higher on Uranus and lower on Neptune (Wenkert et al. 2022). In the next section, we explore other radiative heat sources that could increase the temperature above the tropopause while maintaining a realistic Bond albedo value (keeping in mind that these values may be overestimated or underestimated).

4. Supplementary heat sources in the stratosphere

4.1. Aerosol and cloud layers

Thermochemical models (Pryor et al. 1992; Baines & Hammel 1994) predict, from the temperature profile and the hydrocarbon abundances (CH_4, C_2H_6, C_2H_2), that a thick methane cloud should be located at ∼1500 hPa and that other hydrocarbons should condense in the lower stratosphere and be optically thin for both planets. Several scenarios of the vertical distribution of clouds and hazes have been proposed for Uranus and Neptune to reproduce observations in different portions of the visible and near-infrared (NIR) spectrum. However, numerous sources of uncertainty exist that make the characterisation of the haze/cloud structure very challenging. These include uncertainties in the spectral dependence of optical properties, in the latitudinal and vertical variation of methane abundance, in seasonal changes of cloud distribution, in the difficulty in seeing the contribution of haze/cloud opacities due to the spectral dominance of methane gas in the NIR and uncertainties linked to the narrow spectral windows of observations. Nevertheless, these studies have established a first-order vertical structure on ice giants.

In the domain of study of our model (between 3000 hPa and 5 Pa), Uranus' atmosphere is thought to comprise at least one optically thin haze layer with a particle mean radius of ∼0.1 µm located above the CH_4 condensation level and an optically thick cloud layer located between 1000 and 3000 hPa with larger particle size (∼1 µm). The existence of the methane cloud layer remains although thermodynamically expected because some scenarios do not need such a cloud at the level of methane condensation (Sromovsky & Fry 2007; Karkoschka & Tomasko 2009; Irwin et al. 2012, 2015; Roman et al. 2018; Sromovsky et al. 2019). Some more complex haze/cloud scenarios with more haze layers exist (Sromovsky & Fry 2007; Sromovsky et al. 2011, 2014). Concerning the optical properties of the haze located in the upper troposphere (Tice et al. 2013; Sromovsky et al. 2014) or the lower stratosphere (Sromovsky & Fry 2007; Karkoschka & Tomasko 2009; Sromovsky et al. 2011; Tice et al. 2013; Irwin et al. 2015, 2017), they are poorly constrained. Moreover, latitudinal variations in optical depth, refractive index and particle radius have been found recently for the upper haze (Sromovsky et al. 2011, 2019; Roman et al. 2018), adding difficulty in identifying the optical properties of haze particles.

Concerning Neptune, a lot of scenarios have also been proposed to reproduce the vertical haze/cloud structure. These studies retrieved a similar vertical haze/cloud structure but optically thinner in comparison to Uranus. The haze particle radii are also found to be smaller (∼0.1 µm) than that of the deep cloud particles (∼1 µm; Karkoschka & Tomasko 2011; Luszcz-Cook et al. 2016; Irwin et al. 2019). As on Uranus, the optical properties are also poorly constrained Karkoschka & Tomasko 2011; Irwin et al. 2011, 2016, 2019; Luszcz-Cook et al. 2016 and the existence and altitude of the tropospheric methane cloud is uncertain (Karkoschka & Tomasko 2011). Due to the intense cloud activity, the retrieved properties from various scenarios are also latitudinally dependent.

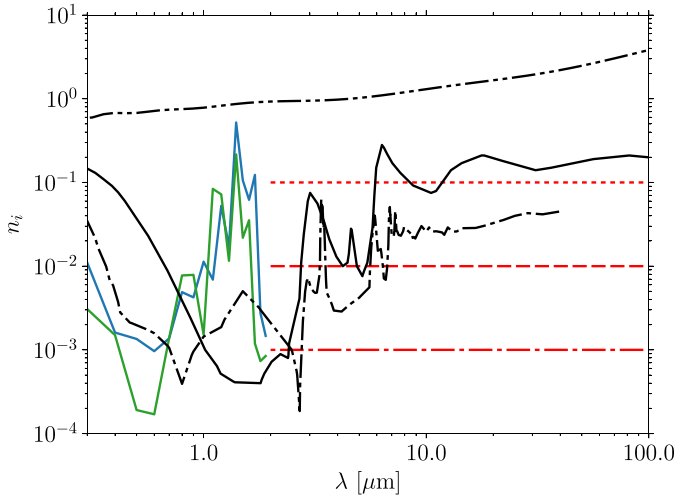

Fig. 3. Uranus: imaginary refractive indices for Uranus. The blue line corresponds to the vertically extended photochemical haze and the green line to the concentrated haze located near the CH_4 condensation level from Irwin et al. (2022). Three different ad hoc values (1×10^{-1}, 1×10^{-2}, 1×10^{-3}) in the thermal infrared (>2 µm) are added (red lines). For reference, refractive indices of tholins (Khare et al. 1984), ice tholins (Khare et al. 1993) and black carbon (Jäger et al. 1998) are also shown in solid, dotted-dashed and double dotted-dashed black lines respectively.

Nearly all these models were based on narrow-band observations, with a limited spectral range. Irwin et al. (2022) reanalysed a combined set of observations (IRTF/SpeX, HST/STIS, Gemini/NIFS) to cover a broader spectral range (0.3–2.5 µm) than other studies in order to better characterise the vertical structure of haze/cloud layers in ice giants and their optical properties from visible to near-infrared light. By using this combined spectrum and a radiative transfer model, the following vertical structure (in the vertical range of our model) has been found for both planets:

- A vertically extended photochemical haze at pressures lower than 1000 hPa composed of submicron-sized particles which are more scattering at visible wavelengths and more absorbing at UV and longer wavelengths (see their imaginary refractive index in Fig. 3 for Uranus and Fig. 4 for Neptune);
- A compact aerosol layer concentrated near the methane condensation level at 1000–2000 hPa composed of micron-sized particles with similar optical properties to the optically thin extended haze above it (see Figs. 3 and 4).

On Neptune, Irwin et al. (2022) added a thin methane cloud layer near the tropopause to fit the reflectance spectrum at wavelengths longer than ∼1 µm. We note that this tropopause cloud is very spatially variable rather than globally uniform, corresponding to the patchy clouds seen in NIR data. Concerning the absence of methane cloud at ∼1000 hPa on Uranus and Neptune, the authors argue that the presence of aerosols at 1000–2000 hPa acting as cloud-condensation nuclei, causes such a rapid condensation of methane that the newly formed methane ice precipitates instantly. Because the study by Irwin et al. (2022) is the most comprehensive one to date, we thus base our aerosol parametrisation on their results.

In our model, the effects of clouds and hazes on radiative heating and cooling rates are simulated using the following inputs: their total optical depth, their vertical distribution

Table 1. Best-fit haze scenario adapted from Irwin et al. (2022) that is consistent with the Bond albedo retrieved during the Voyager 2 flyby (Pearl et al. 1990; Pearl & Conrath 1991).

Haze/cloud layer	Parameter	Uranus	Neptune
Vertically extended photochemical haze	Bottom pressure (hPa) p_1	1600	1600
	Fractional scale height f_1	2.0	2.0
	Optical depth (at 0.8 µm) τ_1	0.04	0.05
	Particle radius (µm) r_1	0.05	0.05
Haze concentrated near CH_4 condensation level	Bottom pressure (hPa) p_2	1500	2000
	Fractional scale height f_2	0.1	0.1
	Optical depth (at 0.8 µm) τ_2	2.0	1.0
	Particle radius (µm) r_2	0.8	0.8
Methane cloud at the tropopause	Bottom pressure (hPa) p_{CH_4}	–	200
	Fractional scale height f_{CH_4}	–	0.1
	Optical depth (at 0.8 µm) τ_{CH_4}	–	0.03
	Particle radius (µm) r_{CH_4}	–	2.5

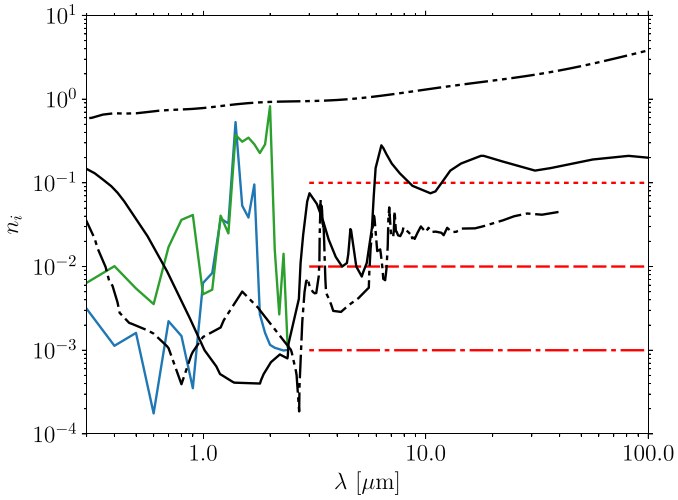

Fig. 4. Same as Fig. 3 but for Neptune.

(parameterised with a given bottom pressure level and a fractional scale height), the weighted mean of their particle radius distribution with their effective variance, and the optical properties of the species. The latter are the extinction coefficient, the single scattering albedo and the asymmetry factor which are calculated by a Mie code (Bohren & Huffman 1983) as a function of wavelength for a given particle radius and refractive index (the real part n_r and the imaginary part n_i). The vertical distribution of the vertically extended photochemical haze on both planets is less constrained. For the next investigations, we adopt the value of the fractional scale height adopted by Irwin et al. (2022) where the aerosols are uniformly present from 1600 hPa to the top of our model (~5 Pa). The reality is necessarily more complex, with a more irregular distribution and an altitude above which the atmosphere is effectively clear of hazes.

For the hazes, the weighted average of all best-fitting retrieved refractive index (n_i) spectra deduced by Irwin et al. (2022) are used, but they are only available in the visible/NIR part of the spectrum. Knowing the refractive index in the thermal infrared is necessary to account for thermal emission from hazes. Thus, three different ad hoc values of refractive index (1×10^{-1}, 1×10^{-2}, 1×10^{-3}) in this spectral range have been tested (Fig. 3 for Uranus and Fig. 4 for Neptune) to estimate the amount of radiative cooling by these hazes. In the case of Neptune, the refractive index from Martonchik & Orton (1994) is used for the additional methane cloud located at the tropopause.

Before evaluating the radiative impact of aerosols on the temperature profile, preliminary tests according to the ranges of the different parameters of these cloud and haze layers (Table 2 in Irwin et al. 2022) are necessary in order to verify if the Bond albedo obtained by our model is consistent with the one retrieved during the Voyager 2 flyby. The best-fit scenario for both planets is given in Table 1 and the Bond albedo from these parameters is 0.35 for Uranus and 0.34 for Neptune, which corresponds for both planets to the upper limit of the Bond albedo retrieved during Voyager 2 era. Knowing that the Bond albedo observed is maybe overestimated on Neptune, the albedo obtained by our model may not be realistic. We note that without the methane cloud layer only at the tropopause, the Bond albedo obtained is equal to 0.29.

We find that including hazes significantly warms Uranus' stratosphere: our simulated temperature profiles for the three different thermal infrared refractive index values closely approximate Voyager 2 observations (Fig. 5). The difference between the simulated temperature without aerosol layers and the observed temperature reached 70 K in the lower stratosphere (~10 Pa). By adding these aerosols, it is only ~5–10 K at this level depending on the value of n_i in the thermal infrared. At the tropopause and lower stratosphere, the thermal structure is now more consistent with the observed tropopause level than the case without haze layers. This difference is explained by the absence of radiative species sufficiently absorbent to warm the atmosphere at these levels. The refractive index of this aerosol layer is fairly high near the ultraviolet and in the near-infrared, and the opacity is high enough for the absorption to be significant to allow heating. The results of our simulations are different from previous publications where it was assumed that aerosols had little or no effect on heating the stratosphere (Marley & McKay 1999; Moses et al. 1995). This will be discussed in Sect. 4.4. However, at pressures below 30 Pa, the heating is no longer sufficient to maintain a profile similar to that observed, due to a lower opacity of the aerosol layer. The profile becomes almost isothermal and departs from the temperature profile observed on Uranus. Another heating source seems to be required at the top of our model to better match the observations. Complementary tests by

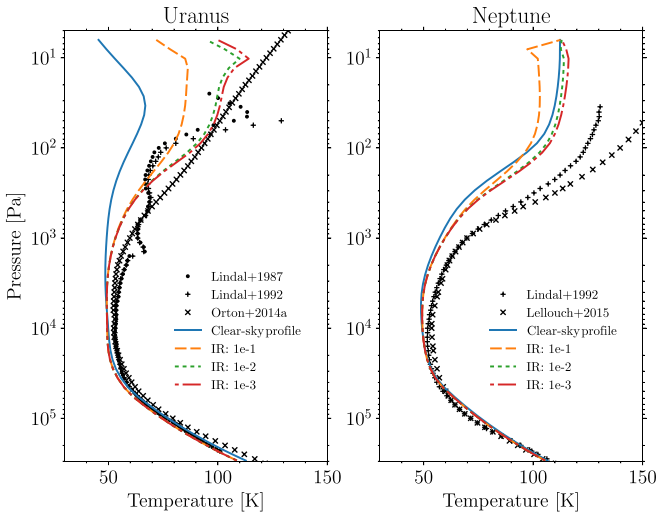

Fig. 5. Simulated temperature profiles of Uranus (left) and Neptune (right) with the Irwin et al. (2022) haze scenario for three different values of the absorption coefficient in the thermal infrared. The dashed orange line is the case with an imaginary index of 10^{-1} in the thermal infrared, the dotted green line is the 10^{-2} case, and the dotted-dashed red line is the 10^{-3} case. For n_i lower than 10^{-3} in the thermal infrared, we obtain the same temperature profile as the case at 10^{-3}. In comparison, the temperature reached without aerosols was added as a blue line and the different observations are shown in black as described in Fig. 1.

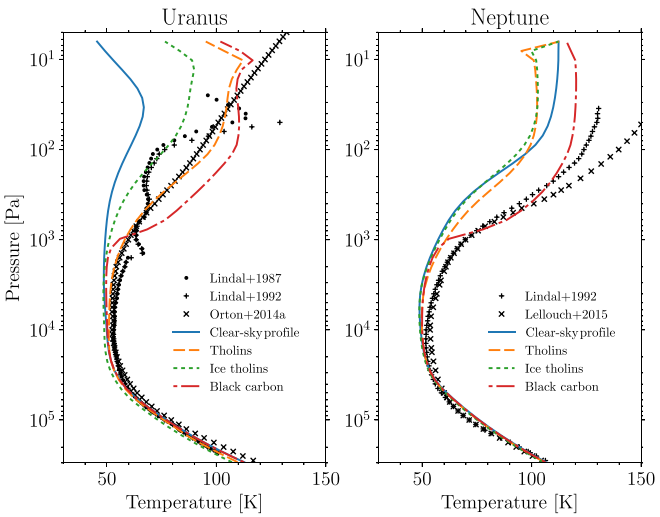

Fig. 6. Simulated temperature profiles of Uranus (left) and Neptune (right) with the Irwin et al. (2022) haze scenario but with different optical indices. The dashed orange line is the case where the Irwin et al. (2022) optical indices were replaced by those of tholins (Khare et al. 1984) and the dotted green line corresponds to ice tholins (Khare et al. 1993). The dotted-dashed red line is the temperature simulated with an ad hoc black carbon dust layer located between 5 and 1000 Pa. In comparison, the temperature reached without aerosols is displayed as a blue line and the different observations are shown in black as described in Fig. 1.

changing the optical indices of aerosol layers by those of tholins and ice tholins were performed. Ice tholins-like particles indeed seem to be a good candidate for the haze (Irwin et al. 2022) as they have similar refractive indexes (Figs. 3 and 4). When using the ice tholins optical indices (Fig. 6), we also report a warming effect but it is less important than when using the haze properties of Irwin et al. (2022). Rather, a similar warming is simulated by our model by replacing the optical indices of Irwin et al. (2022) by those of tholins.

In the case of Neptune, the heating produced by aerosol layers is in a relative sense less important than the one obtained on Uranus (Fig. 5) because absorption in near-infrared light is already dominated by methane in the stratosphere (unlike Uranus). Adding the aerosol scenario only adds 5 K compared to the simulation without aerosol at ∼1 hPa. Moreover, assuming the highest value for n_i in the thermal infrared yields a net cooling effect for $p < 1$ hPa due to a large thermal emission. At pressures above the 1 hPa level, the temperature becomes also almost isothermal. By replacing the optical indices by tholins or ice tholins, no significant change is observed (Fig. 6).

Another interesting candidate for the haze material is the rings of these planets. UVS observations showed that the hydrogen exosphere of Uranus extends to the rings and therefore can transport dust materials into the atmosphere (Broadfoot et al. 1986; Herbert et al. 1987). Rizk & Hunten (1990) showed that dust particles falling from rings in a small latitude band centred at the equator can significantly warm the high stratosphere of Uranus. The particles from the rings are known to be very dark, similar to black carbon (Ockert et al. 1987; Karkoschka 1997). We performed tests by adding an arbitrary haze layer with optical constants of black carbon retrieved in laboratory from a pyrolysis experiment (Jäger et al. 1998) without the haze scenario from Irwin et al. (2022). An optically thin ($\tau = 0.01$ at 160 nm) layer of this type of particle with a small radius (0.1 µm) confined arbitrarily between 1000 and 5 Pa can warm this entire vertical range. The Bond albedo of 0.27 obtained is consistent with the value calculated during the Voyager 2 era (0.30±5). Adding this layer on Neptune gives a similar warming (Fig. 6) but the optical depth must be greater than on Uranus ($\tau = 0.05$ at 160 nm). This greater opacity means that the atmosphere is darker, with a Bond albedo equal to 0.22, inconsistent with the observed value (0.29±5). Moreover, such a ring-flowing material on Neptune remains speculative due to the lack of observations of an exosphere extending to the rings.

Similarly to West et al. (1991) and Marley & McKay (1999), we find that ethane (C_2H_6), acetylene (C_2H_2) and diacetylene (C_4H_2) ices are insufficiently dark in the UV and visible and too optically thin to absorb significant amounts of solar flux on both planets by using Baines & Hammel (1994) haze scenario. Acetylene haze has an anti-greenhouse effect and results in a decrease in temperature by 5–10 K on Uranus. This haze could be responsible for the low temperature observed between 70 and 300 Pa. On Neptune, no significant effect is visible.

4.2. Stratospheric methane abundance

The abundance of methane is rather poorly constrained on both planets. We explore the impact of the methane abundance on our simulated profile to assess if the mismatch between models and observations could be solved by setting a specific methane abundance within current observational errors.

Various estimates of the methane abundance obtained in Uranus' atmosphere are summarised in Fig. 7. The general observed trend is a strong decrease above the tropopause level, where methane decreases from typically $\sim 10^{-4}$ at 100 hPa to below 10^{-6} at the 1 hPa level. This trend is qualitatively reproduced by the seasonal photochemical model of Moses et al. (2018, 2020), although that model significantly exceeds the methane abundance derived from Voyager 2/UVS by Yelle

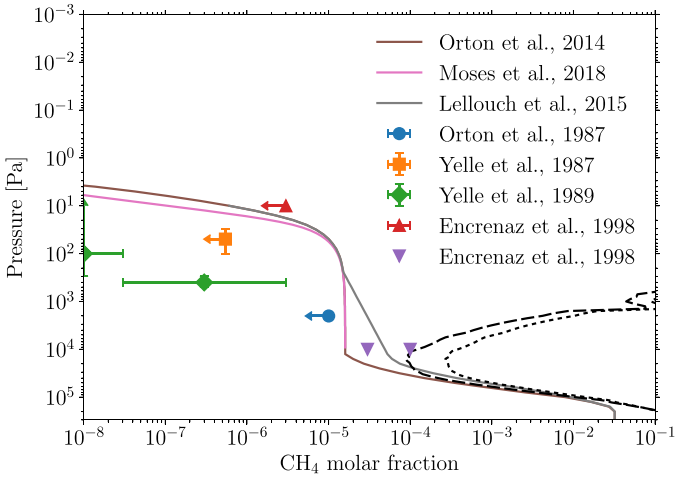

Fig. 7. Methane volume mixing ratio in the atmosphere of Uranus estimated by different observations and models. The dotted line represents the liquid saturated CH_4 vmr calculated from Lindal et al. (1987) temperature profile and the dashed line is the ice saturated CH_4 vmr. The nominal CH_4 vmr profile used in our model is Lellouch et al. (2015) below the 100 Pa level and Moses et al. (2018) above the 100 Pa level.

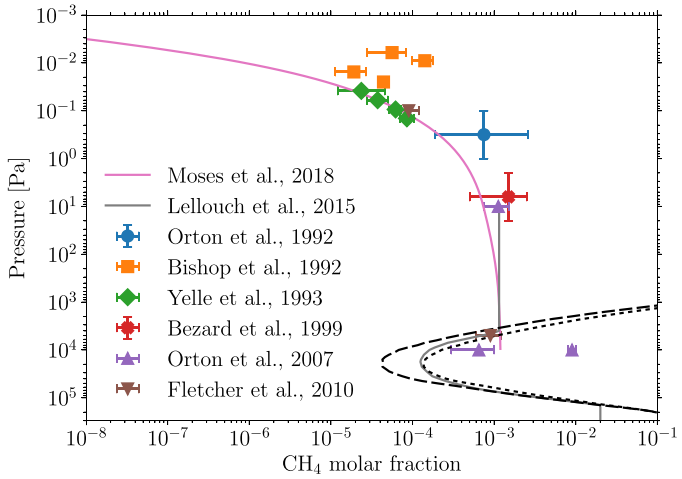

Fig. 8. Methane volume mixing ratio in the atmosphere of Neptune retrieved by different observations and models. The dotted line represents the liquid saturated CH_4 vmr calculated from Lindal (1992) temperature profile and the dashed line is the ice saturated CH_4 vmr. The CH_4 vmr profile used in our model is Lellouch et al. (2015) between 1500 and 100 hPa from and Moses et al. (2018) above 100 hPa level. Below the 1500 hPa, the CH_4 vmr value from Irwin et al. (2019) is assumed.

et al. (1987, 1989) at 1–10 hPa. Assuming a lower value of the eddy diffusion coefficient in the photochemical model (hence resulting in a lower homopause level) can match the UVS methane data. However, this results in a strong underestimation of the acetylene abundance derived from UV/visible spectrum and thermal infrared (see discussion in Moses et al. 2005 and references therein). This suggests that the homopause level may vary with latitude and/or season, or that the methane abundances derived from UVS were strongly underestimated. Measurement discrepancies in the methane abundance are also found in the lower stratosphere, where Lellouch et al. (2015) derived a volume mixing ratio (vmr) equal to 9.2×10^{-5} near 100 hPa from Herschel far infrared and sub-mm observations (compatible with analyses of ISO measurements by Encrenaz et al. 1998), while the analysis of *Spitzer*/InfraRed Spectrograph (*Spitzer*/IRS) observations by Orton et al. (2014) is consistent with a much smaller abundance, of 1.6×10^{-5}, at that pressure level.

For Neptune, several estimations of the stratospheric CH_4 vmr profile exist (Fig. 8). From ground-based spectroscopic infrared observations, CH_4 vmr estimations below the 1 Pa level and above the tropopause seem to be in agreement with each other with a value of $\sim 1 \times 10^{-3}$. At lower pressures, a discrepancy between observations appears. From Voyager 2/UVS solar occultation lightcurves, Bishop et al. (1992) constrained the abundance of methane to be in the range $0.2–1.5 \times 10^{-4}$ between 0.006 and 0.025 Pa. However, with the same dataset, Yelle et al. (1993) derived almost the same values but at higher pressures (~0.1 Pa). Using the disk-averaged infrared spectra obtained by Akari, Fletcher et al. (2010b) derived a similar value at this pressure level. The photochemical model from Moses et al. (2018) is also consistent with the latter estimations of CH_4 vmr at this level and also reproduces the CH_4 vmr estimated in the low stratosphere.

The nominal methane profile used in our model consists in the Lellouch et al. (2015) profile below the 100 Pa level for Uranus (1000 Pa for Neptune) and Moses et al. (2018) above it. On Neptune, the methane tropospheric value is set to 4% following Irwin et al. 2019). However, the aforementioned discrepancies in different observed methane values in the lower stratosphere and/or in the homopause altitude level (Figs. 7 and 8) leave room to test other methane profiles and evaluate their influence on the temperature profile. We also test unrealistically high methane abundance profiles to evaluate what would be the amount of methane needed to match the observed temperatures. For Uranus, tests were carried out by multiplying by 2, 4, 6, 8 and 10 our nominal case of CH_4 vmr above the methane condensation level, with the constraint of never exceeding CH_4 local liquid saturation. The highest methane abundance tested for Uranus is similar to the mean CH_4 vmr retrieved on Neptune's lower stratosphere. In the case of Neptune, the methane homopause level is already above the top of the model (~5 Pa). So, only tests by multiplying the CH_4 vmr above the a priori methane condensation level have been done without exceeding CH_4 local liquid saturation on Neptune (Fig. 8).

The tests presented in this section have been made without any haze/cloud layers. Results obtained with different values of methane abundance show that the stratosphere of Uranus is highly sensitive to the amount of methane (Fig. 9). A value of 10^{-4} for the CH_4 vmr throughout the lower stratosphere, which corresponds to a saturated case at the tropopause, can sufficiently warm these levels to match the observations. This amount is too large compared to the globally averaged observations (Lellouch et al. 2015; 3–10 times higher depending on the pressure level). One could argue the possibility of a greater local methane abundance at the location of the Voyager 2 radio-occultation profile. However, the globally averaged temperature being similar to the Voyager 2 temperature, this assertion is unlikely but strong and temporal methane gradients as for C_2H_2 (Roman et al. 2022) can exist. Supplementary tests have been made by increasing only the homopause of the nominal profile from 100 to 10 Pa by maintaining the vertical gradient between 100 and 200 Pa. A warming has been observed but it remained confined to the last levels of our model (for pressures lower than ~50 Pa). The Bond albedo obtained for all abundances tested is similar to the clear-sky Bond albedo (see Sect. 3).

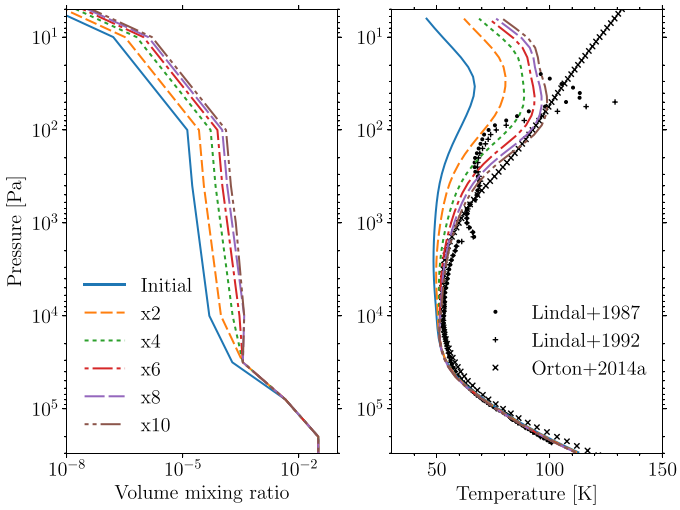

Fig. 9. Simulated temperature profiles with different methane abundances on Uranus. Left: CH_4 vmr profile (solid blue line, see Sect. 3), with two (short dashed orange curve), four (dotted green curve), six (dotted-dashed red curve), eight (long dashed violet curve), and ten (double dotted-dashed maroon curve) times the nominal abundance. Right: the corresponding simulated temperature profiles. The black symbols are the observed temperatures described in Fig. 1.

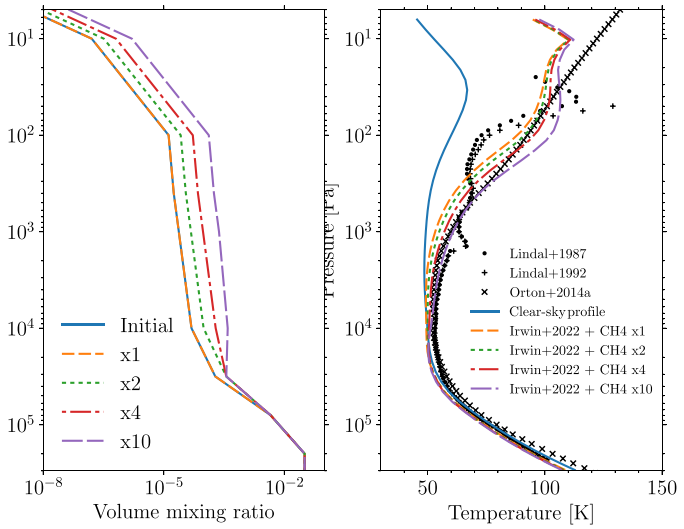

Fig. 10. Simulated temperature profiles with different abundance of methane on Uranus with the Irwin et al. (2022) haze scenario. Left: CH_4 vmr profile on Uranus (blue line and short dashed orange line) or with that abundance multiplied by a factor of two (dotted green line), four (dotted-dashed red line), ten (long dashed violet line). Right: the corresponding simulated temperature profiles. The solid blue line corresponds to the clear-sky model (see Sect. 3) with a nominal CH_4 vmr profile. The black symbols are the observed temperatures described in Fig. 1.

By adding the best-fit haze/cloud scenario, the amount of additional methane necessary to warm the stratosphere is much less important, or even not needed considering that the temperature simulated only with the cloud model is already close to the Voyager 2 profiles. An amount 2–4 times higher than our reference profile, still consistent with the range of observations (Fig. 10), enables the temperature profile of Voyager 2 to be matched. Thus, a higher abundance of methane can partly account for the warm observed temperatures on Uranus.

In any of the tested scenarios described above, the combination of haze/cloud scenarios and various methane abundance profiles remain insufficient to reproduce the observed temperature on Uranus at pressures lower than 30 Pa. An additional heating is required at the top of the model to reduce the gap between the simulated temperature and the observed one.

On Neptune, the atmosphere is far less sensitive to the addition of higher methane amounts (Fig. 11) at any level because the spectral windows of the methane are already saturated. To be close to the observed temperature, the methane abundance would have to be 100 times greater than that measured. Thus, a higher methane abundance cannot be the solution to the energy crisis on Neptune, even with additional heating from aerosol.

4.3. Thermospheric conduction

The thermospheres of Uranus and Neptune are well-known for the energy crisis problem. The temperature expected from solar heating is inconsistent with the observed ones at these levels (Melin et al. 2019). A temperature of 750 K has been measured at the expected level of the thermopause by UV stellar and solar occultations on Uranus (Broadfoot et al. 1986) and UV solar occultation on Neptune (Broadfoot et al. 1989) during the flyby of Voyager 2. Since then, a significant and constant decrease in temperature, based on several measurements of H_3^+ from ground-based observations, has been observed on Uranus (Melin et al. 2019). Since 1992, the cooling rate was 8K per terrestrial year such that in 2018, the temperature reached 486 K. In the case

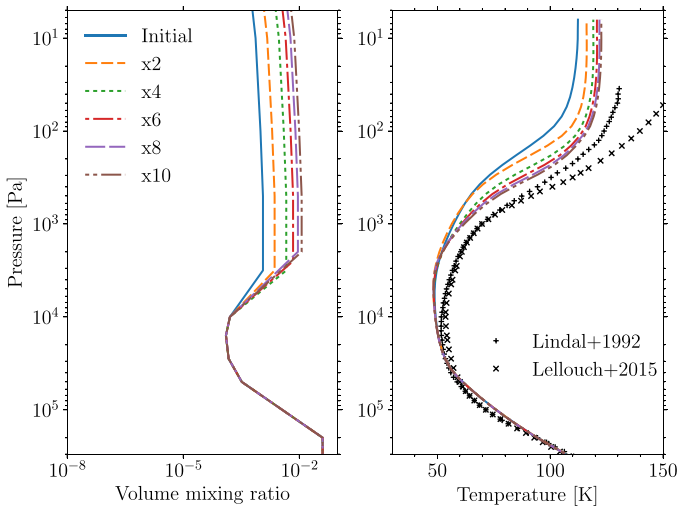

Fig. 11. Simulated temperature profiles with different methane abundances on Neptune. Left: CH_4 vmr profile on Neptune with the nominal CH_4 vmr profile (solid blue line, see Sect. 3), or with that abundance multiplied by two (short dashed orange curve), four (dotted green curve), six (dotted-dashed red curve), eight (long dashed violet curve), and ten (double dotted-dashed maroon curve) above the methane condensation level. Right: the corresponding simulated temperature profiles. The black symbols correspond to the observed temperatures described in Fig. 1.

of Neptune, no measurement of the thermospheric temperature has been made since the Voyager 2 flyby. However, Moore et al. (2020) suggest from H_3^+ upper limits and models that the upper atmosphere may have significantly cooled since the Voyager 2 era. In any case, the thermosphere is warmer than expected. Atomic and molecular hydrogen being inefficient radiators, the heat energy on the thermosphere is lost by radiative cooling of

Table 2. Heat fluxes tested for Uranus and Neptune as a function of the temperature range in the thermosphere and the thickness of this layer.

Name	ΔT (K)	Δz (km)	$Q_{c,bottom}$ (W m^{-2})
UC1	170–500	1100	6.5×10^{-5}
UC2	150–500	260	2.62×10^{-4}
UC3	150–500	50	1.36×10^{-3}
NC1	150–750	1450	1.07×10^{-4}
NC2	150–750	10	1.56×10^{-2}

Notes. For Uranus, two values of conductivity were tested (see text). $Q_{c,top}$ corresponds to the value of conduction flux at the top of the thermosphere and is equal to 0.

H_3^+ and is carried downwards by conduction to lower levels. Our model does not cover the thermosphere. However, the stratosphere of both planets is contiguous to the warm thermosphere and thus their upper part can be warmed by conduction.

The heat flux Q_c resulting from the thermospheric conduction is approximated as

$$Q_c = -k\frac{\Delta T}{\Delta z}, \quad (1)$$

where k is the thermal conduction coefficient of the atmosphere, ΔT is the temperature range over a thickness Δz located between the bottom and the top of the thermosphere. The thermal conduction coefficient k is calculated by the semi-empirical formula from Mason & Saxena (1959) for a gas mixture of orthohydrogen, parahydrogen at equilibrium and helium using data from Mehl et al. (2010) and Hurly & Mehl (2007). From these results, an interpolation formula expressed as $k = AT^S$ is used to determine the conduction flux from the thermosphere to add at the top of our model. Between 20 and 200 K, the coefficient A is equal to 1.064×10^{-3} J m^{-1} s^{-1} K$^{-(S+1)}$ and S to 0.906.

To determine the Q_c flux at the bottom of the thermosphere, we need to estimate the temperature gradient in the thermosphere, above our model top. In the case of Uranus, two temperature gradients have been tested on the basis of the available observations (Table 2). The first one (UC1) corresponds to the values deduced from stellar and solar occultations by Broadfoot et al. (1986; reworked by Melin et al. 2019). The second gradient (UC2) is that obtained by Herbert et al. (1987), also derived from stellar and solar occultations during the Voyager 2 flyby. In the first case, the conductive flux obtained is equal to 5.90×10^{-8} W m^{-2} km^{-1} whereas in the second case, the conductive flux is much higher due to a greater temperature gradient (1.00×10^{-6} W m^{-2} km^{-1}). Unrealistic cases were tested in order to assess the conductive flux required to heat the stratosphere and bring the observed temperatures and the simulated ones into agreement. On Uranus, a conductive flux of 1.36×10^{-3} W m^{-2} (UC3), corresponding to a thermospheric gradient of +7 K.km^{-1}, is required, and in the case of Neptune, the flux must reach 1.56×10^{-2} W m^{-2} (NC2), corresponding to a temperature gradient of +60 K.km^{-1} in the thermosphere.

For Neptune, the influence of thermospheric conduction is much less plausible according to observations. Indeed, for the pressures considered above our model top, between 10 and 0.04 Pa (Yelle et al. 1993), there is a vertically thick isothermal temperature zone (stratopause) but poorly constrained. It is only for pressures below 0.04 Pa that we enter the thermosphere with a positive temperature gradient. If we disregard this isothermal zone, the conduction flux resulting from this gradient is equal to 7.38×10^{-8} W m^{-2} km^{-1} (model NC1 in Table 2).

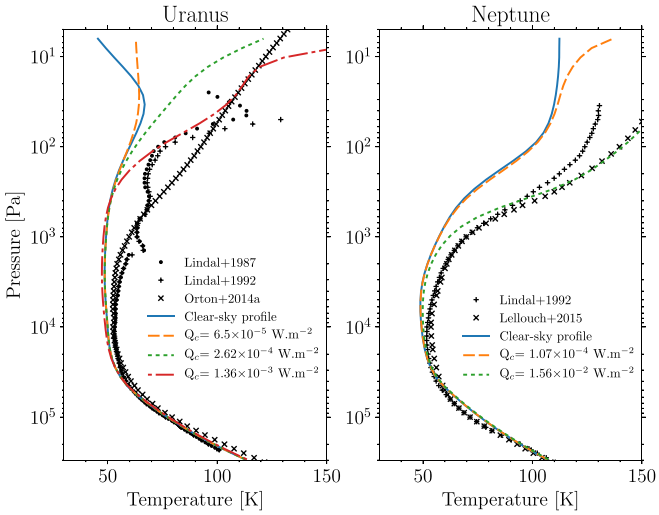

Fig. 12. Scenario with no hazes including heat conduction. Left: simulated temperature profiles on Uranus for the UC1 (dashed orange curve), UC2 (dotted green curve) and UC3 (dotted-dashed red curve) thermospheric conduction scenarios. Right: simulated temperature profiles on Neptune for NC1 (dashed orange curve) and NC2 (dotted green curve) thermospheric conduction scenario. The solid blue line is the clear-sky model (Sect. 3). The black symbols are the observed temperatures described in Fig. 1.

From these heat fluxes, the heating rate from thermospheric conduction is parameterised as follows:

$$\frac{\partial T}{\partial t} = \frac{1}{\rho c_p}\frac{\partial}{\partial z}\left(k\frac{\partial T}{\partial z}\right) \quad (2)$$

with c_p the specific heat capacity at constant pressure, ρ the density. The thermospheric conduction flux is fixed at the last level of our model where the formula can be rewritten as

$$\frac{\Delta T}{\Delta t} = \frac{1}{\rho c_p}\frac{Q_{c,bottom}}{\Delta z}. \quad (3)$$

On Uranus, in the case without aerosols (Fig. 12), the top of our model (at pressures below 50 Pa) is sensitive to a conductive heat flux. All cases show that the thermospheric conduction cannot warm levels below the 50 Pa level on Uranus and Neptune. This is expected, as the vertical temperature gradient becomes very small and as radiative effects start to dominate heat exchanges at these levels. In the UC2 case, the temperature gain obtained from heat conduction on the last pressure level (5 Pa) of our model is 70 K while it is of the order of 10K in the UC1 case. With aerosols (Fig. 13), the UC2 scenario allows the temperature to be increased by 15 K at the top of the model and to keep a more realistic temperature gradient in the upper stratosphere. Concerning Neptune, the atmosphere remains insensitive to such a flux except on the top of our model (for pressures below 10 Pa). Moreover, the methane already dominates radiative exchanges at these pressure levels (unlike Uranus, where the methane homopause resides at much higher pressures). The same is true by adding the aerosol scenario. In any case, thermal conduction cannot be a solution to the energy crisis in the middle stratosphere of Neptune. In addition, the thermospheric conduction creates a temperature gradient in the upper stratosphere inconsistent with the isothermal zone present above the 10 Pa level (Yelle et al. 1993).

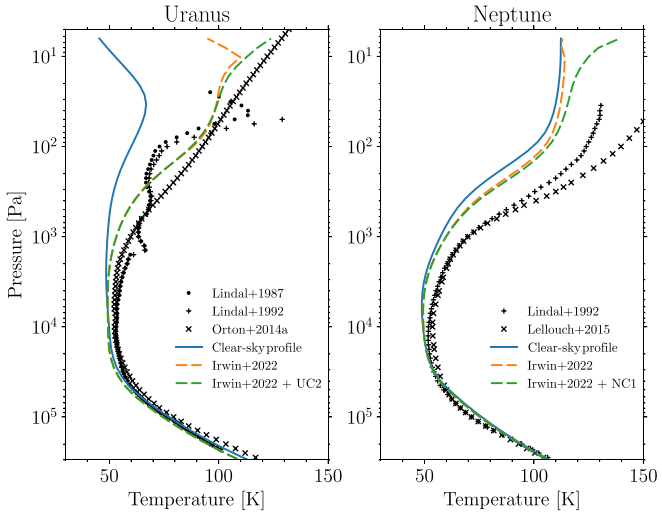

Fig. 13. Scenario with hazes including heat conduction. Left: simulated temperature profiles on Uranus with the Irwin et al. (2022) haze scenario but no conduction (long-dashed orange line) and with haze and thermospheric conduction with the UC2 flux scenario (dashed green line). Right: same for Neptune (but with the NC1 flux scenario for the dashed green line). The solid blue line is the clear-sky case (Sect. 3) and the black symbols are the observed temperatures described in Fig. 1.

4.4. Discussion

Previous radiative–convective models (Appleby 1986; Friedson & Ingersoll 1987; Wang 1993; Marley & McKay 1999; Greathouse et al. 2011; Li et al. 2018) failed to correctly reproduce the temperature profile observed by Voyager 2 without additional heat sources. They all featured a temperature profile from the tropopause to the stratosphere that was too cold compared to the data, like our clear-sky profile on Uranus and Neptune (Fig. 1).

Adding more methane in the stratosphere was one of the first hypotheses considered as the missing heat source for these two planets, especially for Neptune. Marley & McKay (1999) investigated this issue on Uranus by setting realistic methane values. Due to poor constraints on the methane abundance on Uranus, a wide range of values were tested. Assuming small abundances of 10^{-7} to 10^{-10} (consistent with the Voyager 2 UVS results by Herbert et al. 1987 and Stevens et al. 1993) in the upper stratosphere (between 3 and 0.3 Pa), they found that methane radiates downwards and warms the atmosphere above 50 Pa by up to 15 K. By using similar values of methane abundance at these levels and without hazes, we reproduce a similar result on Uranus where an increase of 10 K at 10 Pa is seen. For the low stratosphere and the tropopause, a CH_4 vmr 10 times higher than observed is necessary to warm these levels in both Marley & McKay (1999) and our simulations. In the case of Neptune, Greathouse et al. (2011) found that an increase of the CH_4 abundance by a factor of 8 was needed to bring the retrieved temperature and the simulated ones into agreement, but in our simulations, an even higher abundance (more than 10 times the observed profile) would be needed (Fig. 11). However, as explained here and by the authors, such a high abundance is inconsistent with respect to previous observations (Lellouch et al. 2010).

With the difficulty of reproducing the observed temperature profile with a realistic methane abundance, the hypothesis of aerosols that absorb the solar flux, locally or globally, was quickly proposed (Appleby 1986; Lindal et al. 1987; Pollack et al. 1987; Bezard 1990; Rizk & Hunten 1990). Appleby (1986) analysed the geometric albedo spectrum from the International Ultraviolet Explorer and found sufficient heating by adding an aerosol layer distributed uniformly between 500 and 3×10^{-2} hPa which absorbed 15% of the total solar irradiance on Uranus. On Neptune, they found that adding an aerosol heating source in the radiative zone does not totally solve the gap between the observed and simulated temperature profiles. However, with the reanalysis by Karkoschka (1994) of the IUE spectrum, Marley & McKay (1999) found that the reanalysed spectrum was inconsistent with the aerosol heating from Appleby (1986).

Marley & McKay (1999) used the haze scenario from Rages et al. (1991) to determine the influence of hazes on the temperature profile of Uranus. They found that the simulated temperature was similar to their 'cold baseline profile' (a case without hazes). This lack of heating by haze in their model may be explained by the assumption of small stratospheric haze particles in the scenario of Rages et al. (1991; decreasing from a radius of 0.05 µm at 500 Pa to 0.01 µm at 40 Pa). This drop in particle size has the effect of favouring scattering rather than absorption at lower pressures. By increasing the imaginary index of refraction of Rages et al. (1991) haze scenario, the aerosols become sufficiently darker in the ultraviolet to warm the stratosphere (Marley & McKay 1999). However, the observed UV geometric albedo is not reproduced (Marley & McKay 1999) and the analysis of a Raman scattered Lyman-α emission in ultraviolet (Yelle et al. 1987) shows that the atmosphere above the 0.5 hPa level seems to be clear on Uranus. Marley & McKay (1999) thus rejected the hazes as a possible solution of the energy crisis on Uranus. The haze scenario from Irwin et al. (2022), which is derived from the analyses of reflected spectra between 0.4 and 2.3 µm, can warm the stratosphere of Uranus and be close to the Voyager 2 profile (Fig. 5) with a particle radius sufficiently large to lead absorption and do not need to be dark in the UV. The low amount of methane in Uranus' stratosphere allows any hazes slightly opaque in the visible and NIR light to be an important heat source, which is not the case on Neptune due to higher amounts of methane. The nature of these hazes is uncertain but could be similar to tholins or ice tholins (Irwin et al. 2022). Using optical constants of tholins instead of those of Irwin et al. (2022) allows one to obtain a similar heating to that produced by Irwin's hazes (Fig. 6). The Bond albedo obtained with the tholins (0.29 for Uranus and 0.27 for Neptune) is also close to the observed values. The Bond albedo calculated with the ice tholins is still consistent with the observations for Neptune (0.33) but for Uranus, the ice tholins reflect too much light (0.38). The real vertical distribution of the stratospheric hazes is also unknown. A more complex vertical structure is expected with local minima and maxima of optical depth and different particle radius (Toledo et al. 2019, 2020). Then, the efficiency of the heating by the aerosols can be different between the layers compared with our simulations. The aerosols may also be organised into bands in the same way as we see for Jupiter and Saturn. On Uranus, several bands have been revealed in near-infrared images (Sromovsky et al. 2015).

On the other hand, we note that Li et al. (2018) raised a problem concerning the presence of oxygen-bearing species like carbon monoxide (Cavalié et al. 2014), which can cool the atmosphere and compensate for other heating sources. This hypothesis was not tested here and its importance has not been determined. Furthermore, in this study, it was hypothesised that

the aerosols were Mie spheres. In the stratosphere of Jupiter, Zhang et al. (2015) showed that fractal aggregate particles produced by coagulation processes dominate the heating at middle and high latitudes contrary to simple Mie aerosol layers. The heating efficiency is better in the case of fractal aggregate hazes because they are optically thinner in the mid-infrared wavelengths and thicker in the UV/visible (Wolf & Toon 2010). A similar configuration of aerosols on ice giants has not been explored yet and would need to be investigated in future studies.

Rizk & Hunten (1990) proposed that dust from the rings falls near the equator, and behaves optically as black carbon. Using some assumptions on opacity, they found that the 0.1–1 Pa layer can be warmed with a carbon-water ice mix. In our model, by extending this layer from the top to 1000 Pa and by using the optical indices of black carbon (Jäger et al. 1998), the dust heating is sufficient to get closer to the temperature observed in the stratosphere not only on Uranus but also on Neptune due its strong absorption continuum in the UV/visible wavelengths. However, this solution suffers from a lack of observation. The concentration, vertical and meridional distribution, particle sizes and their full optical properties remain poorly constrained. Furthermore, as explained by Rizk & Hunten (1990), the ring particles fall only at the equator and can explain the warming only in this region. The dust particles would need to be advected from the equator to high latitudes to warm all the stratosphere.

The effect of thermospheric conduction on stratospheric heating has been little studied to date. For Uranus, Marley & McKay (1999) managed to heat the upper stratosphere by 9 K by adding thermospheric conduction (profile B1) to their baseline profile (profile B). They note that conduction has an effect on the temperature profile only for pressures below 50 Pa and that its efficiency is sensitive to the abundance of methane in the thermosphere, as in our simulations. Unfortunately, their study does not focus on the values of conductive flux at the top of the model. We can only see that the addition of conduction allows the upper stratosphere to be heated, but in a weak to moderate way, as observed in our simulations. The effect of thermospheric conduction on the stratosphere remains uncertain on Uranus due to the uncertainties on the thermospheric temperature gradient. On the one hand, ground-based stellar occultations have shown significant temperature variability in this atmospheric region (Baron et al. 1989; Young et al. 2001). On the other hand, measurements during the Voyager 2 flyby are inconsistent by several hundred Kelvins compared with ground-based occultations (Saunders et al. 2023). In the case of Neptune, Wang (1993) found that conduction had no influence for levels deeper than 10 Pa. We also agree with this finding because methane absorption dominates the heating rates below this level.

To summarise, while the Uranian temperature profile can be reproduced with our 1D radiative–convective equilibrium model (with a realistic haze scenario), none of the heat sources investigated here can properly warm Neptune's stratosphere. The answer to the energy crisis on Neptune may lie in its dynamical activity. Important temperature fluctuations have been seen from ground-based stellar occultations in the high stratosphere and low thermosphere of Neptune. Roques et al. (1994) identified these fluctuations as the manifestation of inertia-gravity waves emanating from the lower atmosphere. They show that inertia-gravity waves dissipation can compete with the radiative heating and cooling rates from methane between 3 Pa and 0.03 Pa. On Uranus, these waves could also play a role. We defer the study of the impact of waves to future work.

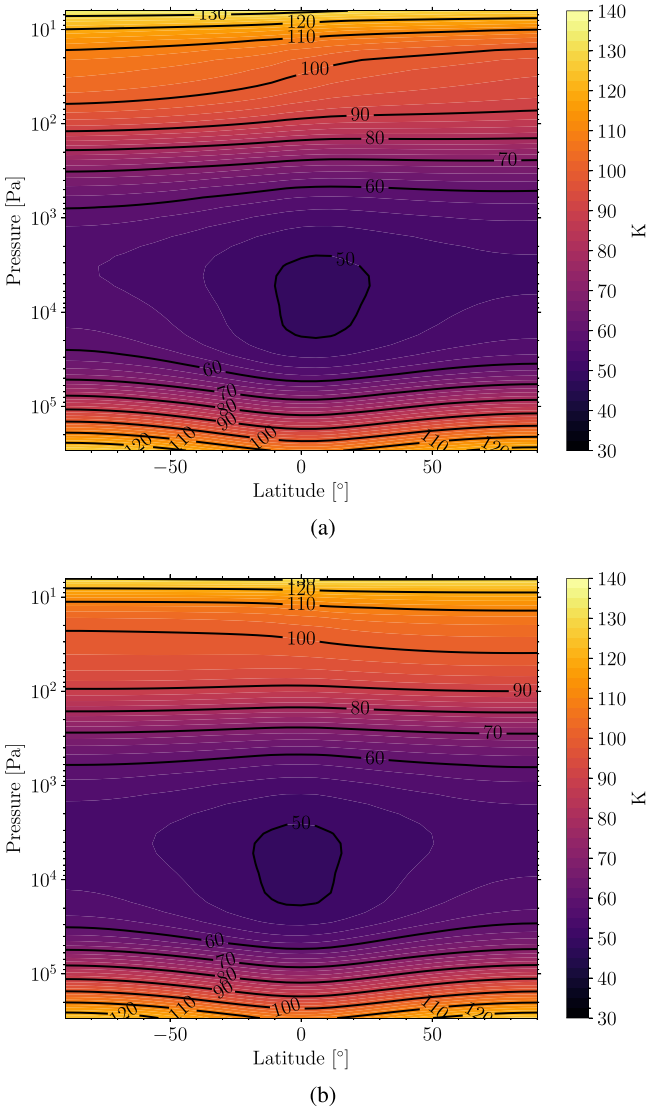

Fig. 14. Uranus: Vertical cross sections of temperature at spring equinox (Ls=0°) (a) and northern summer solstice (Ls=90°) (b). The temperature observed at autumn equinox and winter solstice is almost similar (because of its slightly non circular orbit) as spring equinox and summer solstice but the maximum and minimum temperature is reversed in latitude (Fig. 15).

5. Seasonal and latitudinal temperature evolution

We describe below the seasonal, 2D latitude-altitude temperature fields obtained at radiative-equilibrium from simulations including the aerosols layers on Uranus and Neptune from Irwin et al. (2022) keeping fixed with time and the thermospheric conduction (UC2 scenario) for Uranus only (Fig. 13). Our model assumes methane and other hydrocarbons are horizontally uniform and unchanged over time.

5.1. Overview of the simulated thermal structure

In our simulation of Uranus' stratosphere, maximum latitudinal contrasts (pole to pole) are found to occur at 10 Pa near Ls ≃ 180° and 0°, during the equinoxes, with a temperature gradient of typically 10 K between northern and southern hemispheres (see Figs. 14a and 15). This is shifted by Ls = +90° following the solstices (Fig. 15) due to its long radiative time constant (Li

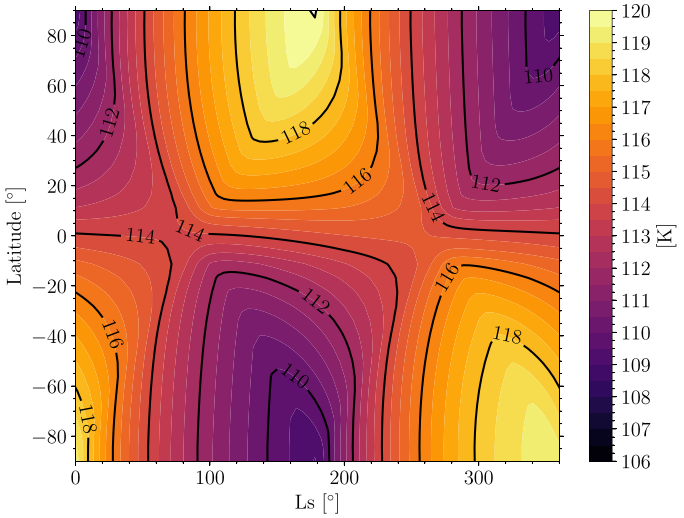

Fig. 15. Evolution of the simulated temperature at 10 Pa on Uranus during one Uranian year.

et al. 2018). The maximum temperature reached at 10 Pa is 119 K and the minimum is 108 K. A small asymmetry is visible between the northern and southern autumn (resp. spring) where the temperature is ∼1.2 K higher (resp. lower) during northern autumn (resp. southern spring). This difference is explained by the eccentricity of Uranus (equal to 0.047) which is high enough to induce a small temperature change. Indeed, the perihelion occurs during the northern autumn equinox (Ls ≃ 182°) where the seasonal contrast is maximum. The minimum seasonal contrast at 10 Pa occurs at Ls ≃ 55° and 250°. Below the 1 hPa level, much lower seasonal temperature contrasts are seen. At and below the tropopause level, temperatures are found to be colder at the equator than at the poles throughout the year, consistent with long radiative timescales and with greater insolation at the poles than at the equator on an annual average due to Uranus' extreme obliquity. On average, at 3000 hPa, the temperature meridional gradient reaches ∼15 K with a maximum of 123 K at the poles and a minimum of 108 K at the equator. Still, small seasonal changes are observed (of the order of a few Kelvins) in the upper troposphere, and the location of the minimum temperature is found to oscillate within ±10° of the equator between the equinoxes.

On Neptune, the maximum seasonal contrast (pole to pole) at 10 Pa is greater than on Uranus due to the higher amount of methane at this level and shorter radiative timescales. The maximum temperature gradient at 10 Pa reaches 27 K between the northern and the southern hemisphere and it occurs at Ls ≃ 140° and 320°, hence +50° following the solstices (see Figs. 16a and 17). This seasonal shift between the solstice and maximum seasonal contrast is similar to that found on Saturn (Guerlet et al. 2014; Fletcher et al. 2010a). Contrary to Uranus (and Saturn), Neptune's small eccentricity (equal to 0.009) does not influence its seasonal forcing (∼0.2 K). The minimum seasonal contrast at 10 Pa occurs near Ls ≃ 30° and 210°. The seasonal temperature contrast becomes insignificant (less than 5 K) at pressures greater than 10 hPa. At the tropopause (∼100 hPa), the minimal temperature is found at high latitudes at the end of winter and beginning of spring, reaching 47 K, and the maximum temperature centred at the equator is at 51 K. In the troposphere, no significant seasonal variation is seen and the equator-to-pole temperature gradient amounts to ∼9 K throughout the year. The

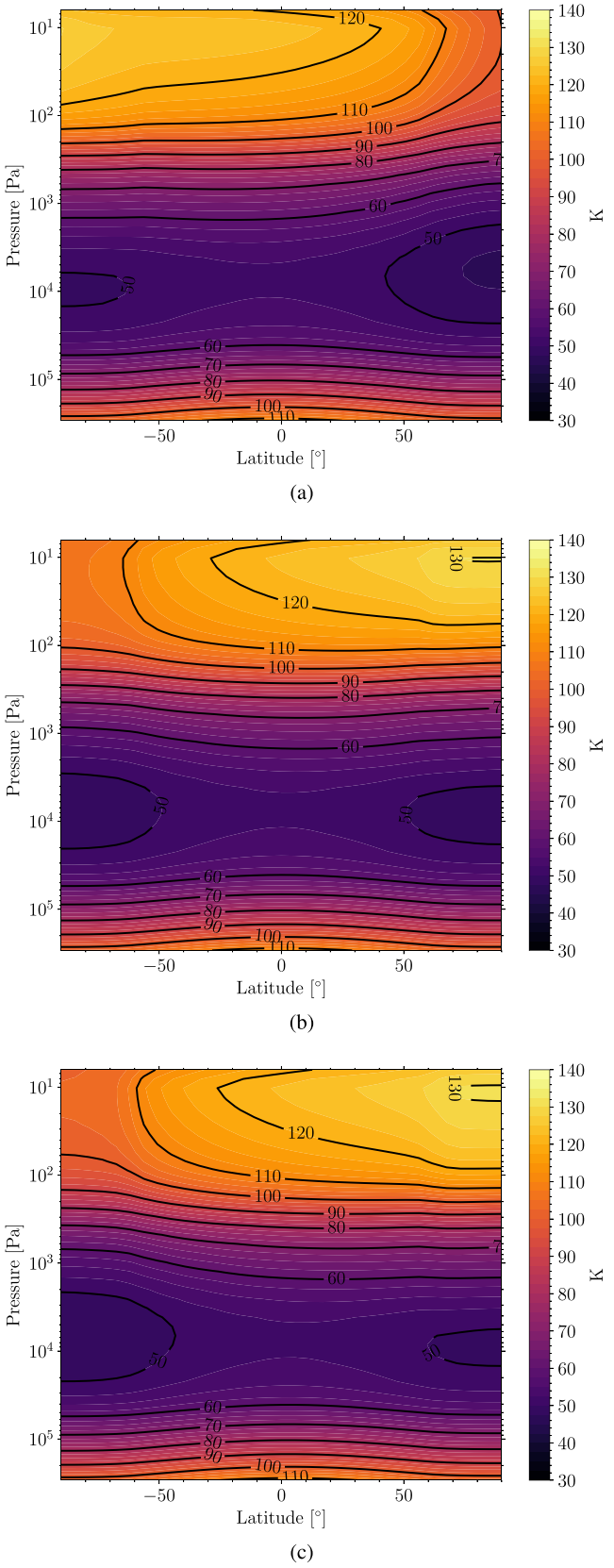

Fig. 16. Neptune: Vertical cross sections of temperature at spring equinox Ls=0° (a), northern summer solstice Ls=90° (b), and during the northern maximum stratospheric temperature contrast at Ls=140° (c). The temperature observed at autumn equinox, winter solstice and the maximum seasonal contrast in the other hemisphere is almost the same but the maximum and minimum temperature is reversed in latitude.

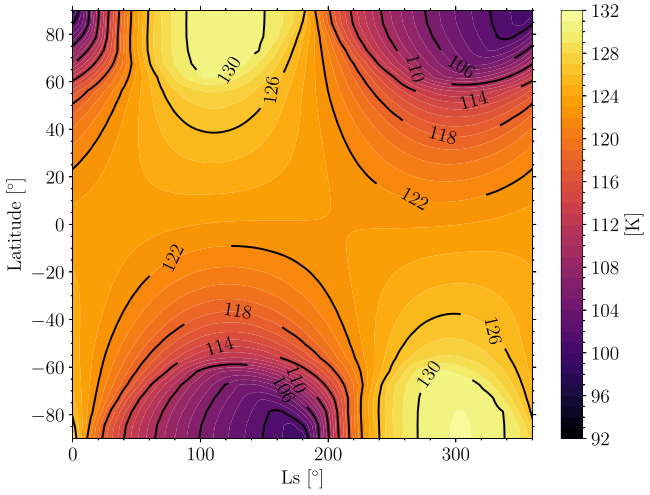

Fig. 17. Evolution of the simulated temperature at 10 Pa on Neptune during one Neptunian year.

maximum temperature at 3000 hPa is 112 K at the equator and the minimum at the poles is equal to 103 K.

5.2. Comparison to previous radiative-convective models

Several radiative-convective models were developed during the Voyager 2 era in order to predict the meridional temperature structure on Uranus and Neptune. All previous models produce seasonal temperature variations on Uranus. Wallace (1983) predicted an annual thermal amplitude of the effective temperature (corresponding to ~300 hPa level) on Uranus of 4.9 K at the poles and 0.4 K at the equator (but with an internal heat flux of 0.32 W m^{-2}). This annual contrast at the poles is similar in the simulation of Bezard (1990), where it amounts to 3.5 K and reaches at most 0.1 K at the equator. In our model, these differences in amplitude between the equator and the poles are also observed (Fig. 18c). An annual contrast of 4.1 K at the poles and 0.6 K at the equator is seen and, the maximum and minimum temperatures occur near the equinoxes (at the same level), like on the model of Wallace (1983) and Bezard (1990). Interestingly, due to the obliquity and the radiative forcing lag, two maxima and minima at the equator are visible (Fig. 18c) at pressures higher than 10 hPa.

On Neptune, the annual thermal amplitude is found to be greater at high latitudes than at the equator, as on Uranus. The Wallace (1984) and Bezard (1990) models give similar results but the amplitudes are very low (1–2 K for the poles and <0.5 K at the equator at ~500 hPa). This is consistent with the annual contrast observed on our model (1.1 K at the poles and <0.1 K at the equator; Fig. 18d). The maximum north-to-south asymmetry occurs after each solstice in our model like on the previous models introduced above. Greathouse et al. (2011) predicts temperature near the winter solstice (Ls ≃ 275°) to be 10 K warmer at the south pole than at the equator in the upper stratosphere (0.12 hPa) and the meridional temperature gradient becomes smaller at deeper levels (2.1 hPa). These previous predictions are in agreement with our simulations (Fig. 16), yet none reproduce observations.

5.3. Comparison to observed temperature contrasts on Uranus

On Uranus, very few spatially resolved observations probing the lower stratosphere have been made, contrary to Neptune (see Sect. 5.4), due to the cold temperatures and hence a poor signal-to-noise ratio. VLT/VISIR mid-infrared images at 13 μm (Roman et al. 2020), sensitive to the pressure level of 25 Pa, revealed that the meridional temperature trend between 20°S and 70°N remained unchanged between 2009 (Ls ≃ 7°) and 2018 (Ls ≃ 43°). They report a minimum temperature centred at the equator and a maximum at mid-latitudes (40°S and 40–60°N). In addition, localised longitudinal temperature variations that may be the manifestation of meteorological activity were reported (Rowe-Gurney et al. 2021). The meridional temperature variations simulated by our model are inconsistent with the observed ones (Roman et al. 2020) in the lower stratosphere. Our radiative equilibrium model predicts a maximum temperature at the south pole and a minimum at the north pole between 7° and 43° in solar longitude (Fig. 15). Concerning the seasonal variations, we predict a temperature increase (resp. decrease) of 3 K at 25 Pa at the north (resp. south) pole between 2009 and 2018, which is at odds with the lack of observed seasonal trends between these two dates (Roman et al. 2020).

The Voyager 2/IRIS experiment provides information about the thermal structure in the upper troposphere, between 70 and 400 hPa at Ls ≃ 271° (Conrath et al. 1998; Orton et al. 2015). In this pressure range, derived temperatures by Orton et al. (2015) show minima at mid-latitudes (30–40°N and 20-–50°S) and maxima at the equator and the poles. Conrath et al. (1998) show only one minimum located at 30°N. The source of the discrepancy between Conrath et al. (1998) and Orton et al. (2015) is unclear (see Orton et al. 2015 for discussion). The thermal structure predicted by our model is however different (Fig. 19): the maximum is located at the poles and the minimum at the equator. However, the maxima and minima predicted at the tropopause are similar to those observed at higher levels, in the lower stratosphere (Roman et al. 2020). Below the 100 hPa level, the temperature on IRIS data appears to be symmetric between the two hemispheres but above this level, a very slight asymmetry is present. At the tropopause (around 70 hPa), there is a temperature difference of 1 K between the two minima at mid-latitudes, with the northern (winter) latitudes exhibiting lower temperatures. This asymmetry could be explained by the eccentricity of Uranus where the perihelion occurs during the northern autumn equinox and IRIS observations were made during the northern winter solstice. However, the 1 K variation is probably within the uncertainties on the IRIS retrievals. A similar temperature anomaly is found in our simulations (Fig. 15) but at higher latitudes and lower pressure. Thermal imaging performed one season after the IRIS observations (during the spring equinox in 2007) showed no significant change in tropospheric temperature between the two hemispheres. But observations after the spring equinox (Roman et al. 2020) show a very slight increase in temperature in the northern and summer hemisphere (<0.3 K). A similar trend is observed in our simulations at the same period near the tropopause.

5.4. Comparison to observed temperature contrasts on Neptune

Contrary to Uranus, more measurements of the stratospheric temperature on Neptune have been made since the Voyager 2 era. Assuming a latitudinally uniform distribution of methane as Greathouse et al. (2011), Fletcher et al. (2014) compare thermal-infrared images from Keck/LWS (2003), Gemini-S/TReCS (2007) and built synthetic images from temperatures derived by IRIS on Voyager 2 (1989). A latitudinally uniform temperature is retrieved both in 1989 (Ls ≃ 235°) and 2007 (Ls ≃ 275°), except

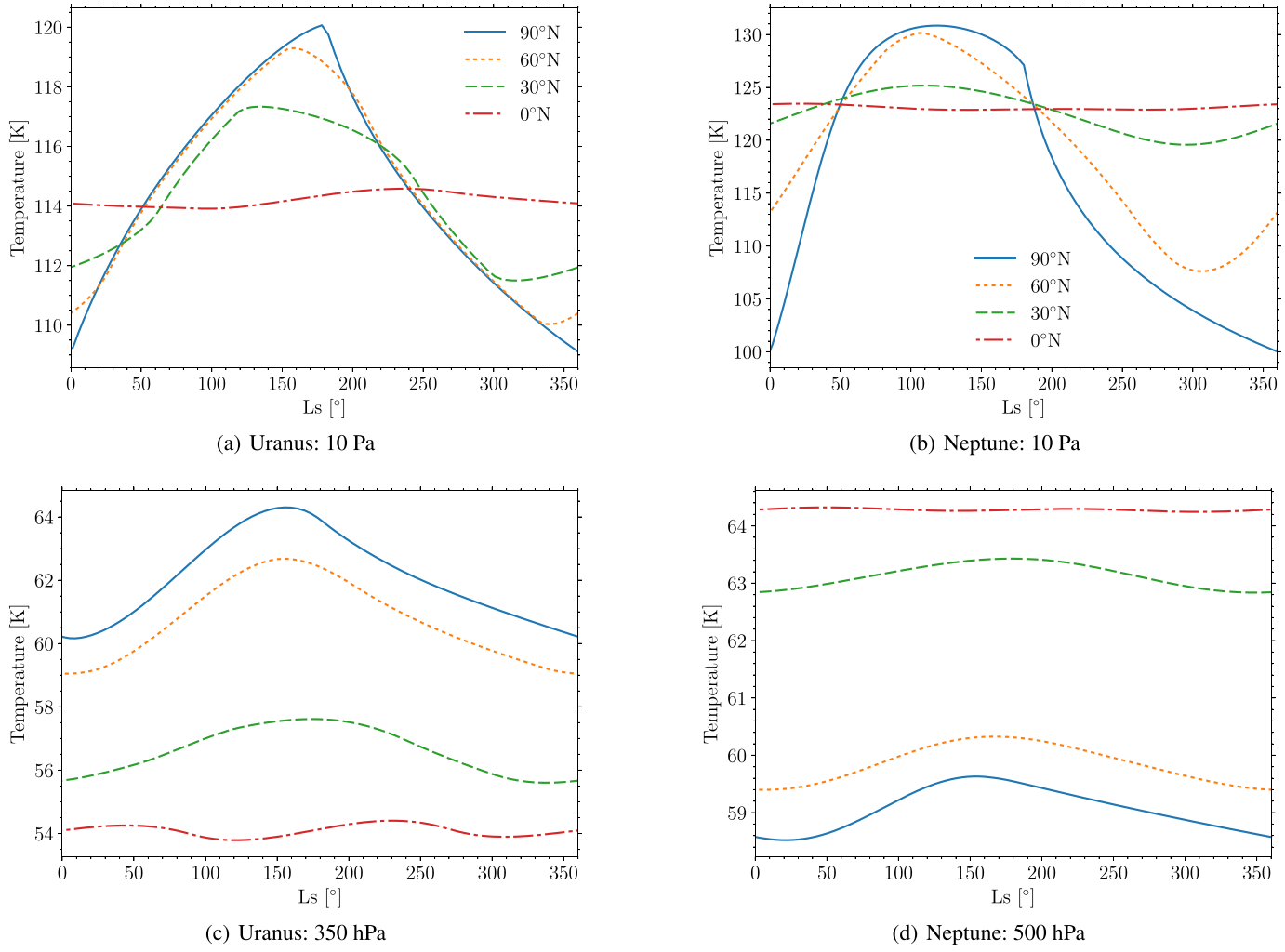

(a) Uranus: 10 Pa

(b) Neptune: 10 Pa

(c) Uranus: 350 hPa

(d) Neptune: 500 hPa

Fig. 18. Evolution of the temperature during one planetary year on Uranus (left) at 10 Pa (a) and 350 hPa (c) and on Neptune (right) at 10 Pa (b) and 500 hPa (d) for a latitude of 90°N (solid blue line), 60°N (dotted orange line), 30°N (dashed green line), and 0° (dashed-dotted red line).

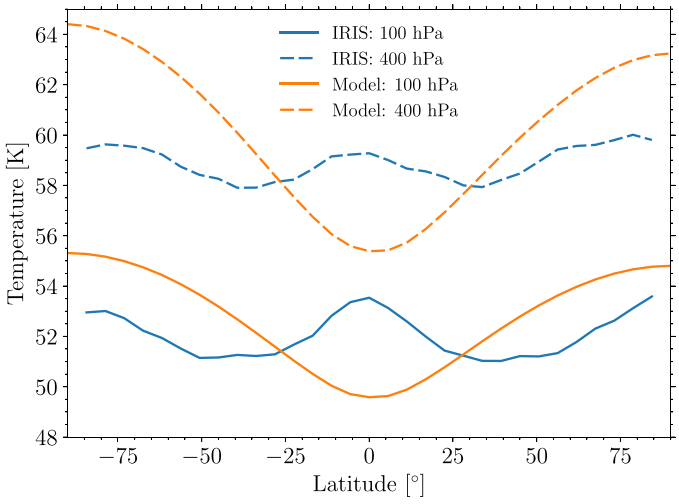

Fig. 19. Uranus: comparison of the temperature retrieved (blue line) from the Voyager 2/IRIS experiment (Orton et al. 2015) and the simulated temperature (orange line) at 100 hPa (solid line) and 400 hPa (dashed line). Uncertainties from the spectral inversion of IRIS data are lower than 1 K.

at the south pole, where a warm polar vortex became evident only after the Voyager 2 flyby. However, stratospheric temperatures inferred between 2003 (Ls ≃ 266°) and 2020 (Ls ≃ 303°) show meridional variations between 0.1 and 0.5 hPa (Roman et al. 2022). In addition, significant temporal variations are highlighted by Roman et al. (2022). Several temperature drops and increases of several Kelvins (1–10 K) are observed during this period. Our simulated temperatures are inconsistent with the observed trends and meridional temperatures. At the solar longitudes of the observations (between 266° and 303°), a minimum is seen at the north pole and a maximum at the south pole as expected for a model with only pure radiative forcing at the southern summer. A warm south pole is observed since at least 2003 (Ls ≃ 266°). Our simulations also predict this warm south pole where the maximum is reached between Ls ≃ 272 and 333° at 0.1 hPa. The simulated temporal evolution of the temperature is much smoother than the observations (Fig. 20): the disk-averaged temperature calculated in our simulation taking the subsolar latitude into account shows a little variation (~2 K maximum) while the observed disk-averaged temperatures present important variations over shorter timescales at all latitudes and pressure levels. We note however that most observations agree with our predicted trends. An exception concerns observations

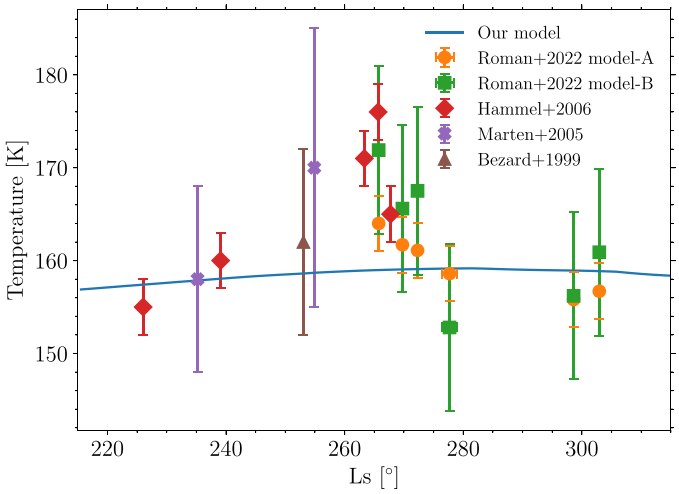

Fig. 20. Comparison of the simulated disk-averaged temperature at 10 Pa on Neptune computed given the subsolar latitude observed from Earth (blue line) and the disk-averaged temperatures retrieved by Bézard et al. (1999) at ∼5 Pa (brown triangle), Marten et al. (2005) at ∼10 Pa (violet cross), Hammel et al. (2006) between ∼10 and 1 Pa (red diamond), and Roman et al. (2022) at ∼10 Pa (green square and orange circle). Due to the global offset in temperature between our simulations and the observations (Fig. 13), we have added +35K to our model results to help compare the trends in the datasets.

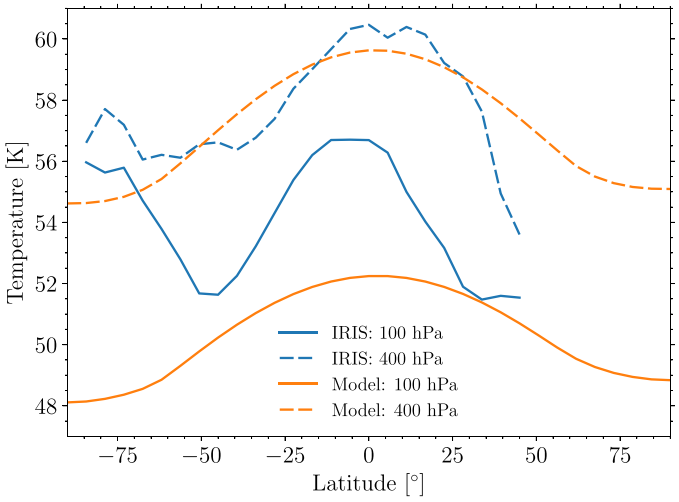

Fig. 21. Neptune: comparison of the temperature retrieved (blue line) from IRIS experiment (Fletcher et al. 2014) and the temperature simulated (orange line) at 100 hPa (solid line) and 400 hPa (dashed line). Uncertainties from the spectral inversion of IRIS data are lower than 1 K.

performed near Ls ≃ 270° by Hammel et al. (2006) where the retrieved temperature significantly exceeds the general trend.

At pressures lower than 0.1 hPa, a quasi-isothermal vertical structure with no temporal variation (less than 3 K) is observed from CH_4 emission (Fletcher et al. 2014) but to be consistent with the temperature retrieved by Greathouse et al. (2011) at 0.007 hPa, this quasi-isothermal layer must be contained between 0.1 and 0.01 hPa. A similar quasi-isothermal vertical temperature is revealed by Roman et al. (2022) but an analogous meridional temperature variation as at deeper levels (0.1 hPa) is seen between 2003 and 2020. This vertically quasi-isothermal layer is also observed in our actual radiative-convective simulation (Fig. 13) at pressures below 1 hPa.

Concerning the upper troposphere, Fletcher et al. (2014) reanalysed IRIS data and retrieved the temperature between 70 and 800 hPa. A complex thermal structure has been revealed by this dataset which is rather similar to Uranus. At the tropopause (100 hPa), a minimum temperature of 51 K is present at mid-latitudes (±45°) and a maximum temperature is reported at the south pole and the equator (56 K). The local minimum temperature in the northern hemisphere is slightly colder and appears to be higher in altitude than its southern counterpart. Due to the geometry of observation, no data beyond 40°N has been obtained. Roman et al. (2022) found that the thermal structure at the tropopause is quite different from that in the stratosphere, on average. The minimum temperature seen at mid-latitudes near the tropopause does not extend to the stratosphere. In our simulation, the maximum temperature near the tropopause is also found at the equator but the south pole is colder and no temperature minimum is found at mid-latitudes (Fig. 21). At 400 hPa, the retrieved temperature seems to be more consistent with our model in the southern hemisphere. Retrievals from mid-infrared spectroscopy observations performed with Keck/LWS in 2003 (Ls ≃ 266°; Fletcher et al. 2014), VLT/VISIR in 2006 (Ls ≃ 272°), 2009 (Ls ≃ 279°) and 2018 (Ls ≃ 299°), Gemini-N/MICHELLE in 2007 (Ls ≃ 270°) and Subaru/Cooled Mid-Infrared Camera and Spectrometer (Subaru/COMICS) in 2008 (Ls ≃ 277°) and 2020 (Ls ≃ 303°) (Roman et al. 2022) show that the temperature is unchanged at these levels since the Voyager 2 encounter, except for the south pole where the hot spot present at the upper troposphere and lower stratosphere (visible at 100 hPa in Fig. 21) seems to be colder since 2018 but this cooling is uncertain. In our simulations, no change in temperature is observed at these pressure levels.

The thermal structure at the tropopause retrieved on Uranus and Neptune are very similar despite a different solar longitude of observations and seasonal forcings (most notably their obliquity). On both planets, the extrema near the tropopause are located at the same latitude band irrespective of the season. The mismatch between the observed thermal structure and the simulated one with our model suggests that the dynamics strongly influences the meridional temperature and is active over long timescales. Flasar et al. (1987) and Conrath et al. (1987) proposed the presence of a mid-latitude upwelling and equatorial subsidence to explain the combination of low temperatures and sub-equilibrium para-fraction, while Karkoschka & Tomasko (2009, 2011) and Sromovsky et al. (2014) proposed an equatorial upwelling to explain cloud formation and the equator-to-pole methane gradient. From the combination of zonal wind, temperature, para-H_2 measurements and the distribution of condensable volatiles, de Pater et al. (2014) and Fletcher et al. (2020) designed a model of the possible meridional circulation in the upper troposphere which reconciles the meridional temperature retrieved from IRIS observations and the meridional methane gradient. Above the methane condensation level, the proposed meridional circulation is ruled by a polar and equatorial subsidence and a mid-latitude upwelling. But below this level, the opposite is suggested by this model (with stacked circulation cells) which could explain the observed CH_4 vmr meridional gradient. The investigations of the meridional circulation on these planets remain to be confirmed with a 3D general circulation model.

In addition, the local minima visible at mid-latitudes may result from the thermal wind balance where if there is a decrease with height of the intensity of zonal jets (Fletcher et al. 2014), the meridional temperature gradients must be in balance with this decay.

If we take the latitudinal variation of methane observed in the troposphere of both planets (Karkoschka & Tomasko 2009, 2011; Sromovsky et al. 2019; Irwin et al. 2019) into account, the meridional temperature profile would be different but would still be far from the observations. On Uranus, this would imply a lower heating at the poles than at the equator, which would reduce or reverse the pole-equator contrast in our simulations. On Neptune, this contrast would be much more pronounced.

Photochemical models predict seasonal variations in hydrocarbon abundances in the stratosphere of ice giants (Moses et al. 2018). These variations could play an important role in heating and cooling in the polar regions, where variations of a factor of 10 are expected on Neptune for example.

6. Summary and conclusions

Radio occultations and the IRIS experiment from the Voyager 2 flyby provided important information about the thermal structure of Uranus and Neptune (Lindal et al. 1987; Lindal 1992; Conrath et al. 1998; Fletcher et al. 2014; Orton et al. 2015). Given the low irradiance, the stratosphere of both planets is warmer than expected and this problem is referred to as the energy crisis (also affecting Uranus' and Neptune's thermospheres). Previous models had difficulty or failed to reproduce the observed stratospheric temperatures. One proposed solution was a higher (but unrealistic) concentration of stratospheric methane above the cold trap coupled with thermospheric conduction from an unknown source. Radiative forcing by aerosols was either not taken into account or if it was, it did not yield significant warming, due to incomplete observational constraints on the optical properties and physical characteristics of aerosol particles.

After the Voyager 2 era, the multiplication of near-infrared and thermal infrared observations has provided better constraints on the atmospheric composition, in addition to the vertical aerosol and cloud structure of these planets and completed the temperature observations. The methane abundance on Uranus and Neptune retrieved by Lellouch et al. (2010, 2015), respectively, are lower in the stratosphere than expected by older models. Moreover, the optical properties of hazes retrieved by several studies show that they are inconsistent with hydrocarbons known to condense on these planets (C_2H_6, C_2H_2, and C_4H_2) according to photochemical models (Moses et al. 2018, 2020; Dobrijevic et al. 2020). The nature of the haze appears to be similar to tholins, with significant absorption in the near-infrared (>1 μm) and more scattering in the visible, except near 300–400 nm.

In our study, these state-of-the-art observational constraints were used to better represent the radiative forcings in the atmospheres of Uranus and Neptune. The radiative-convective equilibrium model previously developed for gas giants (Guerlet et al. 2014, 2020) was adapted here to the ice giants, firstly with only the contribution from the gaseous species. As expected, the radiative–convective model without additional heat sources produced the same results as previous models, that is, an important gap between the simulated temperature profile and the observed one (~70 K on Uranus at 0.1 hPa and ~25 K at 1 hPa on Neptune). To match the simulated profile to the observed one, several heat sources have been (re-)investigated. Altogether, our investigations have allowed us to make the following conclusions:

– The haze scenario from Irwin et al. (2022) can reconcile the simulated temperature profile and the one observed by Voyager 2 on Uranus. The heating produced by the hazes is sufficient to reduce the previous gap of 70 K to 5–10 K at 0.1 hPa. Changing the refractive index retrieved by Irwin et al. (2022) to the one of tholins (Khare et al. 1984) allows for a significant warming of the temperature profile, while warming by ice tholins is not sufficient (Khare et al. 1993). Very dark particles similar to dust particles falling from rings can also heat the stratosphere of Uranus, but they seem inconsistent with respect to the haze scenario from Irwin et al. (2022). Concerning Neptune, the simulated temperature with the haze scenario from Irwin et al. (2022) becomes 10 K warmer than the case without aerosols. However, this is still too cold in comparison to the observed temperature profile. Unlike Uranus, no significant change has been obtained if the refractive index is replaced by that of tholins or ice tholins. With a hypothetical haze layer composed of very dark particles, the stratosphere of Neptune can be warmed significantly. The Bond albedo resulting from adding the Irwin et al. (2022) aerosol layers is 0.35 on Uranus and 0.34 on Neptune, consistent with the upper limit set by Pearl et al. (1990) and Pearl & Conrath (1991). Replacing them with tholins' optical constants gives a similar Bond albedo;
– With a larger amount of stratospheric methane, it is possible to warm the temperature profile for both planets as was found in previous studies (Appleby 1986; Marley & McKay 1999). However, the methane abundance necessary to sufficiently warm the temperature profile is inconsistent with observations (Lellouch et al. 2010, 2015). A CH_4 vmr of the order of ten times higher without hazes (or four times higher with hazes) on Uranus and 100 times higher on Neptune in the stratosphere is needed (with or without hazes). Bond's albedo resulting from this greater methane abundance remains almost unchanged compared with the clear-sky model;
– Thermospheric conduction cannot warm the stratosphere alone on both planets as confirming previous studies (Wang 1993; Marley & McKay 1999). Nevertheless, in combination with hazes or a larger amount of methane, conduction allows us to better match the observed temperature profile on Uranus in the upper levels of our model (for pressures below 50 Pa). On Neptune, the effect of conduction is hardly noticeable. The difficulty to warm the stratosphere of Neptune by radiative forcing or conduction leads us to hypothesise that the heating source may have a dynamical origin.

We note that the impact of haze and cloud layers on the heating rates has been investigated with the assumption of Mie scattering theory (spherical particles). However, a more complex structure such as fractal aggregate particles would be worth testing in future studies. Zhang et al. (2015) do indeed show that this type of particle dominates the heating rates in the stratosphere of Jupiter. We cannot yet test this hypothesis in the absence of retrieved haze properties assuming fractal aggregates.

Other heat sources not investigated in this study could also warm the stratosphere, such as heat released by inertia-gravity waves dissipation (Roques et al. 1994). Auroral heating could also heat the upper atmosphere of outer planets. Brown et al. (2020) and O'Donoghue et al. (2021) show that for Saturn and Jupiter, respectively, this process can inject a huge amount of energy about the magnetic poles. However, due to their dominant zonal circulation, the redistribution of heat towards lower latitudes remains difficult to explain. O'Donoghue et al. (2021) find that planetary wave drag can advect the heat from the pole to the equator. The magnetic poles of Uranus are located at ±30° in latitude and ±43° for Neptune. It would also be interesting to study the link with solar activity (Roman et al. 2022).

The IRIS experiment on board Voyager 2 provided key information about the latitudinal thermal structure on these planets. Near the tropopause, the observed temperature is found minimal at mid-latitudes and maximal at the equator and poles on both planets. Surprisingly, despite different radiative forcing (owing to their obliquity and different solar longitude at the date of observation), their thermal structure is relatively similar. By analysing the temperature simulated in our model, two main conclusions can be drawn:

– The simulated meridional thermal structure is inconsistent with the one observed by Voyager 2 at the same solar longitude on Uranus and Neptune and also by ground-based observations. The location of minima and maxima are at odds between our simulations and the observations. For Uranus, the simulated temperature near the tropopause is quite in agreement with the one retrieved from the IRIS experiment at high latitudes. However, the local temperature maximum at the equator was not produced by our model. On Neptune, the temperature at the tropopause is only consistent at the equator. The origin of the observed local maxima and minima could be explained by a meridional circulation which consists in subsidence at the equator and poles (adiabatic warming) and upwelling at mid-latitudes (adiabatic cooling) as proposed by Fletcher et al. (2020) and by thermal wind balance;
– In our simulations, a seasonal variation was seen above the tropopause where the maximum latitudinal contrast was shifted by Ls = +90° following the summer solstice on Uranus and +50° on Neptune. Below the tropopause, very slight variations were simulated on both planets, consistently with long radiative timescales. Contrary to simulations, no significant seasonal change has been observed since the Voyager 2 flyby at the tropopause and lower stratosphere on Uranus (Roman et al. 2020). On Neptune, significant variations in temperature have been observed since the Voyager 2 flyby (Roman et al. 2022). These variations cannot be explained by fully radiative seasonal forcings and suggest other effects with a subseasonal trend. This may indicate that the dynamics control the thermal structure at these levels, or that the assumption of a latitudinally uniform methane abundance and aerosol distribution in the lower stratosphere is not appropriate.

Recent and future observations from *James Webb* Space Telescope should provide new information on the thermal structure of Uranus' and Neptune's troposphere and stratospheres with the Mid-InfraRed Instrument (MIRI) spectrometer and potentially on their haze physical properties and spatial distribution with the Near-Infrared Spectrograph (NIRSPEC) and the Near-InfraRed Camera (NIRCam; Norwood et al. 2016). First spectroscopic observations performed as part of a Guaranteed Time Observation programme (PI: Leigh Fletcher) took place in January 2023 for Uranus and June 2023 for Neptune in the thermal infrared with MIRI. At that time, Uranus was close to the summer solstice (Ls ≃ 64°) and Neptune's season corresponds to southern summer (Ls ≃ 310°). At 0.1 hPa, the thermal contrast predicted from our 1D seasonal model on Uranus is 2.2 K between the equator and the north pole and 7.1 K for Neptune between the equator and the south pole. These new observations will enhance our knowledge of the thermal structure and its variations over time on these planets, and will help to constrain and complete future seasonal radiative-convective models. At the same time, the development of GCMs that take atmospheric dynamics into account appears necessary, given the puzzles that remain regarding the link between their thermal structure and meridional circulation.

Acknowledgements. G. Milcareck, S. Guerlet and A. Spiga acknowledge funding from Agence Nationale de la Recherche (ANR) project SOUND, ANR-20-CE49-00009-01. The authors acknowledge also Jan Vatant d'Ollone for his contribution at an early stage of this project. T. Cavalié acknowledges funding from CNES. Fletcher and Roman were supported by a European Research Council Consolidator Grant (under the European Union's Horizon 2020 research and innovation programme, grant agreement no. 723890) at the University of Leicester.

References

Appleby, J. F. 1986, Icarus, 65, 383
Appleby, J. F. 1990, Icarus, 85, 355
Baines, K. H., & Hammel, H. B. 1994, Icarus, 109, 20
Baron, R. L., French, R. G., & Elliot, J. L. 1989, Icarus, 78, 119
Bezard, B. 1990, Adv. Space Res., 10, 89
Bézard, B., Romani, P. N., Feuchtgruber, H., & Encrenaz, T. 1999, ApJ, 515, 868
Bishop, J., Atreya, S. K., Romani, P. N., Sandel, B. R., & Herbert, F. 1992, J. Geophys. Res., 97, 11681
Bohren, C. F., & Huffman, D. R. 1983, Absorption and Scattering of Light by Small Particles (New York, USA: Wiley-Interscience)
Borysow, A. 1991, Icarus, 92, 273
Borysow, A., & Frommhold, L. 1986, ApJ, 304, 849
Borysow, A., & Frommhold, L. 1987, ApJ, 318, 940
Borysow, A., & Frommhold, L. 1989, ApJ, 341, 549
Borysow, A., Frommhold, L., & Moraldi, M. 1989, ApJ, 336, 495
Borysow, A., Borysow, J., & Fu, Y. 2000, Icarus, 145, 601
Broadfoot, A. L., Herbert, F., Holberg, J. B., et al. 1986, Science, 233, 74
Broadfoot, A. L., Atreya, S. K., Bertaux, J. L., et al. 1989, Science, 246, 1459
Brown, Z., Koskinen, T., Müller-Wodarg, I., et al. 2020, Nat. Astron., 4, 872
Burgdorf, M., Orton, G. S., Davis, G. R., et al. 2003, Icarus, 164, 244
Cavalié, T., Moreno, R., Lellouch, E., et al. 2014, A&A, 562, A33
Conrath, B., Gautier, D., Hanel, R., Lindal, G., & Marten, A. 1987, J. Geophys. Res., 92, 15003
Conrath, B., Flasar, F. M., Hanel, R., et al. 1989, Science, 246, 1454
Conrath, B. J., Gierasch, P. J., & Leroy, S. S. 1990, Icarus, 83, 255
Conrath, B. J., Gautier, D., Lindal, G. F., Samuelson, R. E., & Shaffer, W. A. 1991, J. Geophys. Res. Suppl., 96, 18907
Conrath, B. J., Gierasch, P. J., & Ustinov, E. A. 1998, Icarus, 135, 501
de Pater, I., Fletcher, L. N., Luszcz-Cook, S., et al. 2014, Icarus, 237, 211
Dobrijevic, M., Loison, J. C., Hue, V., Cavalié, T., & Hickson, K. M. 2020, Icarus, 335, 113375
Encrenaz, T., Feuchtgruber, H., Atreya, S. K., et al. 1998, A&A, 333, L43
Flasar, F. M., Conrath, B. J., Gierasch, P. J., & Pirraglia, J. A. 1987, J. Geophys. Res., 92, 15011
Fletcher, L. N., Achterberg, R. K., Greathouse, T. K., et al. 2010a, Icarus, 208, 337
Fletcher, L. N., Drossart, P., Burgdorf, M., Orton, G. S., & Encrenaz, T. 2010b, A&A, 514, A17
Fletcher, L. N., de Pater, I., Orton, G. S., et al. 2014, Icarus, 231, 146
Fletcher, L. N., Gustafsson, M., & Orton, G. S. 2018, ApJ, 235, 24
Fletcher, L. N., de Pater, I., Orton, G. S., et al. 2020, Space Sci. Rev., 216, 21
Friedson, J., & Ingersoll, A. P. 1987, Icarus, 69, 135
Goody, R., West, R., Chen, L., & Crisp, D. 1989, JQSRT, 42, 539
Greathouse, T. K., Richter, M., Lacy, J., et al. 2011, Icarus, 214, 606
Guerlet, S., Spiga, A., Sylvestre, M., et al. 2014, Icarus, 238, 110
Guerlet, S., Spiga, A., Delattre, H., & Fouchet, T. 2020, Icarus, 351, 113935
Halsey, G. W., Hillman, J. J., Nadler, S., & Jennings, D. E. 1988, JQSRT, 39, 429
Hammel, H. B., Lynch, D. K., Russell, R. W., et al. 2006, ApJ, 644, 1326
Hansen, J. E., & Travis, L. D. 1974, Space Sci. Rev., 16, 527
Herbert, F., Sandel, B. R., Yelle, R. V., et al. 1987, J. Geophys. Res., 92, 15093
Hourdin, F., Le van, P., Forget, F., & Talagrand, O. 1993, J. Atmos. Sci., 50, 3625
Hurly, J. J., & Mehl, J. B. 2007, J. Res. Natl. Inst. Stand. Technol., 112, 75
Irwin, P. G. J., Teanby, N. A., Davis, G. R., et al. 2011, Icarus, 216, 141
Irwin, P. G. J., de Bergh, C., Courtin, R., et al. 2012, Icarus, 220, 369
Irwin, P. G. J., Tice, D. S., Fletcher, L. N., et al. 2015, Icarus, 250, 462
Irwin, P. G. J., Fletcher, L. N., Read, P. L., et al. 2016, Icarus, 264, 72
Irwin, P. G. J., Wong, M. H., Simon, A. A., Orton, G. S., & Toledo, D. 2017, Icarus, 288, 99
Irwin, P. G. J., Toledo, D., Braude, A. S., et al. 2019, Icarus, 331, 69
Irwin, P. G. J., Teanby, N. A., Fletcher, L. N., et al. 2022, J. Geophys. Res. (Planets), 127, e07189
Jäger, C., Mutschke, H., & Henning, T. 1998, A&A, 332, 291
Karkoschka, E. 1994, Icarus, 111, 174
Karkoschka, E. 1997, Icarus, 125, 348
Karkoschka, E., & Tomasko, M. 2009, Icarus, 202, 287
Karkoschka, E., & Tomasko, M. G. 2011, Icarus, 211, 780
Khare, B. N., Sagan, C., Arakawa, E. T., et al. 1984, Icarus, 60, 127

Khare, B. N., Thompson, W. R., Cheng, L., et al. 1993, Icarus, 103, 290
Lane, A. L., Hord, C. W., West, R. A., et al. 1986, Science, 233, 65
Lellouch, E., Hartogh, P., Feuchtgruber, H., et al. 2010, A&A, 518, L152
Lellouch, E., Moreno, R., Orton, G. S., et al. 2015, A&A, 579, A121
Li, C., Le, T., Zhang, X., & Yung, Y. L. 2018, JQSRT, 217, 353
Lindal, G. F. 1992, AJ, 103, 967
Lindal, G. F., Lyons, J. R., Sweetnam, D. N., et al. 1987, J. Geophys. Res., 92, 14987
Luszcz-Cook, S. H., de Kleer, K., de Pater, I., Adamkovics, M., & Hammel, H. B. 2016, Icarus, 276, 52
Margolis, J. S. 1993, JQSRT, 50, 431
Marley, M. S., & McKay, C. P. 1999, Icarus, 138, 268
Marten, A., Matthews, H. E., Owen, T., et al. 2005, A&A, 429, 1097
Martonchik, J. V., & Orton, G. S. 1994, Appl. Opt., 33, 8306
Mason, E. A., & Saxena, S. C. 1959, J. Chem. Phys., 31, 511
Massie, S. T., & Hunten, D. M. 1982, Icarus, 49, 213
Mehl, J. B., Huber, M. L., & Harvey, A. H. 2010, Int. J. Thermophys., 31, 740
Melin, H., Fletcher, L. N., Stallard, T. S., et al. 2019, Philos. Trans. Roy. Soc. Lond. Ser. A, 377, 20180408
Moore, L., Moses, J. I., Melin, H., Stallard, T. S., & O'Donoghue, J. 2020, Philos. Trans. Roy. Soc. Lond. Ser. A, 378, 20200100
Moses, J. I., Rages, K., & Pollack, J. B. 1995, Icarus, 113, 232
Moses, J. I., Fouchet, T., Bézard, B., et al. 2005, J. Geophys. Res. (Planets), 110, E08001
Moses, J. I., Fletcher, L. N., Greathouse, T. K., Orton, G. S., & Hue, V. 2018, Icarus, 307, 124
Moses, J. I., Cavalié, T., Fletcher, L. N., & Roman, M. T. 2020, Philos. Trans. Roy. Soc. Lond. Ser. A, 378, 20190477
Norwood, J., Hammel, H., Milam, S., et al. 2016, PASP, 128, 025004
Ockert, M. E., Cuzzi, J. N., Porco, C. C., & Johnson, T. V. 1987, J. Geophys. Res., 92, 14969
O'Donoghue, J., Moore, L., Bhakyapaibul, T., et al. 2021, Nature, 596, 54
Orton, G. S., Fletcher, L. N., Moses, J. I., et al. 2014, Icarus, 243, 494
Orton, G. S., Fletcher, L. N., Encrenaz, T., et al. 2015, Icarus, 260, 94
Pearl, J. C., & Conrath, B. J. 1991, J. Geophys. Res., 96, 18921
Pearl, J. C., Conrath, B. J., Hanel, R. A., Pirraglia, J. A., & Coustenis, A. 1990, Icarus, 84, 12
Pollack, J. B., Rages, K., Pope, S. K., et al. 1987, J. Geophys. Res., 92, 15037
Pryor, W. R., West, R. A., Simmons, K. E., & Delitsky, M. 1992, Icarus, 99, 302
Rages, K., Pollack, J. B., Tomasko, M. G., & Doose, L. R. 1991, Icarus, 89, 359
Rey, M., Nikitin, A. V., Bézard, B., et al. 2018, Icarus, 303, 114
Rizk, B., & Hunten, D. M. 1990, Icarus, 88, 429
Roman, M. T., Banfield, D., & Gierasch, P. J. 2018, Icarus, 310, 54
Roman, M. T., Fletcher, L. N., Orton, G. S., Rowe-Gurney, N., & Irwin, P. G. J. 2020, AJ, 159, 45
Roman, M. T., Fletcher, L. N., Orton, G. S., et al. 2022, Planet. Sci. J., 3, 78
Roques, F., Sicardy, B., French, R. G., et al. 1994, A&A, 288, 985
Rowe-Gurney, N., Fletcher, L. N., Orton, G. S., et al. 2021, Icarus, 365, 114506
Saunders, W. R., Person, M. J., Withers, P., French, R. G., & Tubthong, C. 2023, Planet. Sci. J., 4, 199
Sromovsky, L. A. 2005, Icarus, 173, 254
Sromovsky, L. A., & Fry, P. M. 2007, Icarus, 192, 527
Sromovsky, L. A., Fry, P. M., & Kim, J. H. 2011, Icarus, 215, 292
Sromovsky, L. A., Karkoschka, E., Fry, P. M., et al. 2014, Icarus, 238, 137
Sromovsky, L. A., de Pater, I., Fry, P. M., Hammel, H. B., & Marcus, P. 2015, Icarus, 258, 192
Sromovsky, L. A., Karkoschka, E., Fry, P. M., de Pater, I., & Hammel, H. B. 2019, Icarus, 317, 266
Stevens, M. H., Strobel, D. F., & Herbert, F. 1993, Icarus, 101, 45
Taylor, R. H., Borysow, A., & Frommhold, L. 1988, J. Mol. Spectrosc., 129, 45
Tice, D. S., Irwin, P. G. J., Fletcher, L. N., et al. 2013, Icarus, 223, 684
Toledo, D., Irwin, P. G. J., Rannou, P., et al. 2019, Icarus, 333, 1
Toledo, D., Irwin, P. G. J., Rannou, P., et al. 2020, Icarus, 350, 113808
Toon, O. B., McKay, C. P., Ackerman, T. P., & Santhanam, K. 1989, J. Geophys. Res., 94, 16287
Turbet, M., Leconte, J., Selsis, F., et al. 2016, A&A, 596, A112
Uckert, K., Chanover, N. J., Olkin, C. B., et al. 2014, Icarus, 232, 22
Wallace, L. 1983, Icarus, 54, 110
Wallace, L. 1984, Icarus, 59, 367
Wang, Y. 1993, PhD Thesis, University of Arizona, USA
Wenkert, D., Deen, R. G., & Bunch, W. L. 2022, in AGU Fall Meeting Abstracts, P32E-1865
West, R. A., Lane, A. L., Hord, C. W., et al. 1987, J. Geophys. Res., 92, 15030
West, R. A., Baines, K. H., & Pollack, J. B. 1991, in Uranus, eds. J. T. Bergstralh, E. D. Miner, & M. S. Matthews (University of Arizona), 296
Wolf, E. T., & Toon, O. B. 2010, Science, 328, 1266
Wordsworth, R. D., Forget, F., Selsis, F., et al. 2010, A&A, 522, A22
Yelle, R. V., Doose, L. R., Tomasko, M. G., & Strobel, D. F. 1987, Geophys. Res. Lett., 14, 483
Yelle, R. V., McConnell, J. C., Strobel, D. F., & Doose, L. R. 1989, Icarus, 77, 439
Yelle, R. V., Herbert, F., Sandel, B. R., Vervack, Ronald J., J., & Wentzel, T. M. 1993, Icarus, 104, 38
Young, L. A., Bosh, A. S., Buie, M., Elliot, J. L., & Wasserman, L. H. 2001, Icarus, 153, 236
Zhang, X. 2023a, ApJ, 957, 20
Zhang, X. 2023b, ApJ, 957, 21
Zhang, X., West, R. A., Irwin, P. G. J., Nixon, C. A., & Yung, Y. L. 2015, Nat. Commun., 6, 10231
Zheng, C., & Borysow, A. 1995, Icarus, 113, 84